

# Microphysics and dynamics of snowfall associated with a warm conveyor belt over Korea

Josué Gehring<sup>1</sup>, Annika Oertel<sup>2</sup>, Étienne Vignon<sup>1</sup>, Nicolas Jullien<sup>3</sup>, Nikola Besic<sup>4</sup>, and Alexis Berne<sup>1</sup>

<sup>1</sup>Environmental Remote Sensing Laboratory, École Polytechnique Fédérale de Lausanne (EPFL), Lausanne, Switzerland

<sup>2</sup>Institute for Atmospheric and Climate Science (IAC), Eidgenössische Technische Hochschule Zürich (ETH), Zurich, Switzerland

<sup>3</sup>Department of Geosciences, University of Fribourg, Fribourg, Switzerland

<sup>4</sup>Centre Météorologie Radar, Météo France, Toulouse, France

**Correspondence:** Alexis Berne (alexis.berne@epfl.ch)

**Abstract.** On 28 February 2018, 57 mm of precipitation associated with a warm conveyor belt (WCB) fell within 21 h over South Korea. To investigate how the large-scale circulation influenced the microphysics of this intense precipitation event, we used radar measurements, snowflake photographs and radiosounding data from the International Collaborative Experiments for Pyeongchang 2018 Olympic and Paralympic winter games (ICE-POP 2018). The WCB was identified with trajectories  
5 computed with analysis wind fields from the Integrated Forecast System global atmospheric model. The WCB was collocated with a zone of enhanced wind speed of up to  $45 \text{ m s}^{-1}$  at 6500 m a.s.l., as measured by a radiosonde and a Doppler radar. Supercooled liquid water (SLW) with concentrations exceeding  $0.2 \text{ g kg}^{-1}$  was produced during the rapid ascent within the WCB. Vertical profiles of polarimetric radar variables show during the most intense precipitation period a peak and subsequent decrease in differential reflectivity as aggregation starts. Below the peak in differential reflectivity, the specific differential  
10 phase shift continues to increase, indicating early riming of oblate crystals and secondary ice generation. We hypothesise that the SLW produced in the WCB led to intense riming. Moreover, embedded updraughts in the WCB and turbulence at its lower boundary enhanced aggregation by increasing the probability of collisions between particles. This suggests that both aggregation and riming occurred prominently in this WCB. This case study shows how the large-scale atmospheric flow of a WCB provides ideal conditions for rapid precipitation growth involving SLW production, riming and aggregation. Future  
15 microphysical studies should also investigate the synoptic conditions to understand how observed processes in clouds are related to the large-scale circulation.

## 1 Introduction

Precipitation is the result of a chain of meteorological processes ranging from the synoptic to the micro scales. In particular for stratiform precipitation, the large-scale flow drives the transport of moisture and lifting of air masses, while microphysics  
20 ultimately determine the growth and fall of hydrometeors, influencing precipitation intensity and accumulation. Therefore understanding the link between large-scale flow and microphysics is paramount to better forecast precipitation. Extratropical

cyclones are the main synoptic-scale features associated with precipitation in the mid-latitudes and produce more than 80 % of the total precipitation in the Northern Hemisphere storm tracks (Hawcroft et al., 2012).

Quasi-Lagrangian analyses of mid-latitude baroclinic storms showed the existence of three distinctive airstreams (Carlson, 1980): the dry intrusion, the cold conveyor belt (Harrold, 1973; Browning, 1990; Schultz, 2001) and the warm conveyor belt (WCB, Green et al., 1966; Harrold, 1973; Browning et al., 1973; Dacre et al., 2019; Wernli and P., 2020). The latter can be defined as a coherent warm and moist airstream rising from the boundary layer to the upper troposphere in about two days (Eckhardt et al., 2004; Madonna et al., 2014). Climatological studies of WCBs have used a simple criterion on the ascent rate of trajectories (e.g. 600 hPa in 48 h, Madonna et al. 2014).

WCBs typically rise from below 900 hPa to about 300 hPa and temperature along this flow typically decreases from above 0 °C to below -40 °C. Therefore, clouds along WCBs feature the whole spectrum from warm clouds to mixed-phase to pure ice clouds (e.g. Joos and Wernli, 2012; Madonna et al., 2014). WCBs are the primary precipitation producing feature in extratropical cyclones (Browning, 1990; Eckhardt et al., 2004) and are responsible for more than 70 % of precipitation extremes in the major storm tracks (Pfahl et al., 2014). However, precipitation and cloud processes also impact the dynamics of extratropical cyclones. Trajectory analyses showed that WCBs experience a strong cross-isentropic ascent due to latent heat release (Madonna et al., 2014), which leads to an increase in potential vorticity (PV) below the maximum diabatic heating level and a decrease above it (Wernli and Davies, 1997). This represents a direct link between microphysics and dynamics. Joos and Wernli (2012) studied the impact of different microphysical processes on the diabatic PV production in WCBs. They suggested that condensation of cloud liquid and depositional growth of snow and ice are the most important diabatic heating processes in WCBs. Joos and Forbes (2016) showed the direct impact of specific microphysical processes on the PV modification in WCBs and the subsequent downstream flow evolution.

Colle et al. (2014) studied the distribution of snow crystal habits within mid-latitude baroclinic storms over Long Island, New York. They observed moderately rimed crystals in the middle of the comma head, while heavy riming was present close to the cyclone centre. They also showed a positive correlation between vertical wind speeds, turbulence and degree of riming by means of Doppler data from a micro rain radar. Overall, this study highlights the spatial structure of microphysics occurring in winter storms and suggests a link between the dynamics of the cyclone and observed snow crystal habits.

Dual-polarisation Doppler (polarimetric) radars are useful to study precipitation microphysics, as they provide information on the hydrometeors' shape, density and phase. For instance, differential reflectivity  $Z_{DR}$ , defined as the logarithmic ratio between the reflectivity factor at horizontal and vertical polarisations ( $Z_H - Z_V$  in dB), is a measure of the reflectivity-weighted axis ratio of the targets (Kumjian, 2013; Bringi and Chandrasekar, 2001). Oblate particles (e.g. raindrops, dendrites) have positive  $Z_{DR}$  values, while prolate ones (e.g. vertically oriented ice in an electric field) exhibit negative  $Z_{DR}$  values.  $Z_{DR}$  also depends on the crystal's dielectric constant, but not on the number concentration. Therefore, large aggregates tend to have small  $Z_{DR}$  (<0.5 dB, Kumjian 2013), primarily because they have a much lower density than solid ice, but also because they tend to be more spherical than pristine crystals. On the other hand, aggregates are much larger than crystals and tend to have higher  $Z_H$  values. Consequently, decreasing  $Z_{DR}$  together with increasing  $Z_H$  towards the ground is a consistent signature of the aggregation process (Schneebeil et al., 2013; Kumjian et al., 2014; Grazioli et al., 2015). Furthermore, the specific

differential phase shift ( $K_{dp}$  in  $^{\circ} \text{ km}^{-1}$ ), which is the range derivative of the total differential phase shift on propagation (i.e. phase difference between the horizontal and vertical polarisation waves propagating forward), is related to the axis-ratio, the density, the number concentration and the size of the targets. Being a lower order moment than  $Z_H$ , it is more influenced by the number concentration, such that a high number concentration of small oblate crystals can lead to an increase of  $K_{dp}$ , while  $Z_{DR}$  will barely be affected. Owing to this wealth of information, polarimetric variables have been extensively used for snowfall microphysical studies (Bader et al., 1987; Andrić et al., 2013; Schneebeli et al., 2013; Moisseev et al., 2015; Grazioli et al., 2015). The pioneering work of Bader et al. (1987) showed that high  $Z_{DR}$  values are associated with large dendritic crystals. More recently, Moisseev et al. (2015) found that enhanced values of specific differential phase ( $K_{dp}$ ) are related to the onset of aggregation, producing early aggregates that can be oblate. Grazioli et al. (2015) suggested that similar peaks in  $K_{dp}$  can result from secondary ice generation (leading to a high number concentration of small anisotropic crystals) or the riming of oblate ice crystals, which increases their density. These studies thoroughly analysed dual-polarisation signatures of snowfall microphysics. However, they did not consider the interactions between large-scale flow and microphysics. Keppas et al. (2018) studied the microphysical properties of a warm front with radar and in situ measurements in clouds. They found that a WCB formed a widespread mixed-phase cloud by producing significant amount of liquid water, which favoured riming and secondary ice generation. However, they did not formally identify WCB trajectories nor did they confirm that the liquid water was produced within the WCB. There is hence a need to better understand how the strong, coherent ascending motion within WCBs influences precipitation microphysics. To this end, a synergy between remote sensing and in situ measurements as well as trajectory analyses is needed.

In this study, we use data from the International Collaborative Experiments for Pyeongchang 2018 Olympic and Paralympic winter games (ICE-POP 2018) campaign to study an extreme snowfall event associated with a WCB over South Korea on 28 February 2018. The location of Pyeongchang on a peninsula at mid-latitudes offers an interesting setting to study the interplay between the synoptic circulation, orographic effects and microphysics. First, the surrounding Yellow Sea and East Sea provide nearby sources of moisture for precipitation, which is particularly relevant for wintertime WCBs (Pfahl et al., 2014). Secondly, WCBs play a crucial role for precipitation over the Korean peninsula: between 80 % and 90 % of extreme precipitation is associated with WCBs in South Korea according to a climatological study by Pfahl et al. (2014). The ICE-POP 2018 dataset includes, among others, multiple frequency radar measurements and high-resolution snowflake photographs. We also make use of the Integrated Forecast System (IFS, ECMWF (2017)) model from the European Center for Medium-Range Weather Forecast to identify WCB trajectories associated with this event.

To understand the role of the WCB during this intense precipitation event in Korea, we will address the following questions:

- What was the synoptic situation leading to this intense snowfall event?
- Which microphysical processes were involved?
- How did the specific flow conditions in the WCB influence the observed microphysics?

The paper is structured as follows. We will first introduce the measurement campaign and data sets in Sect. 2. The synoptic situation is presented in Sect. 3. Section 4 shows the evolution of the event over Pyeongchang. An analysis of the microphysics

observed by radar and snowflake images during succeeding periods of interests is presented in Sect. 5. We then summarise the key findings of this study with a conceptual model in Sect. 6 before concluding in Sect. 7.

## 2 Measurement campaign and data set

ICE-POP 2018 was a measurement campaign organised by the Korea Meteorological Administration and supported by the World Meteorological Organisation. Figure 1 shows the location of Pyeongchang and the measurement sites. One of the main goals of ICE-POP 2018 is to improve our understanding of orographic precipitation in the Taebaek mountains (the mountain range along the east coast of the Korean peninsula in Fig. 1). To this purpose remote sensing and in situ measurements of cloud and precipitation were conducted in the Pyeongchang and Gangneung provinces between November 2017 and May 2018. In this study, we will focus on the data collected by an X-band Doppler dual-polarisation radar (hereafter MXPo1), a W-band Doppler cloud profiler (hereafter WProf) and a multi-angle snowflake camera (hereafter MASC), details of which are provided in the following subsections. In addition, we will use measurements from a Pluvio<sup>2</sup> weighing rain gauge located in the Mayhills site (MHS, Fig. 1). Finally, we will show radiosondes (3-hourly resolution) and temperature measurements from Daegwallyeong (DGW) located 2 km away from MHS.

### 2.1 X-band Doppler dual-polarisation radar

MXPo1 was installed on top of a building in the Gangneung Wonju National University (GWU) at the coast of the East Sea (Fig. 1). MXPo1 operates at 9.41 GHz with a typical angular resolution of  $1^\circ$ , range resolution of 75 m, non-ambiguous range of 28 km and a Nyquist velocity of  $39 \text{ m s}^{-1}$  in dual-pulse pair (DPP) mode or  $11 \text{ m s}^{-1}$  in fast-Fourier transform (FFT) mode (see Schneebeli et al., 2013 for more details). The scan cycle was composed of three hemispherical range height indicators (RHIs) at  $225.8^\circ$  (in FFT),  $233^\circ$  (in DPP) and  $325.7^\circ$  (in DPP) azimuth. The first two are towards MHS, while the third is perpendicular to this direction following the coast (red dashed lines in Fig. 1). The RHIs were performed with a range resolution of 75 m and an extent of 27.2 km. The cycle was completed by one plan position indicator (PPI) in DPP mode at  $6^\circ$  elevation (red dashed circle in Fig. 1) and one PPI in FFT mode at  $90^\circ$  elevation (for  $Z_{DR}$  monitoring). The PPI at  $6^\circ$  elevation had a range resolution of 75 m and an extent of 28.4 km. The scan cycle had a 5 min duration and was repeated indefinitely. The main variables retrieved from MXPo1 measurements are the reflectivity factor at horizontal polarisation  $Z_H$  (dBZ),  $Z_{DR}$  (dB),  $K_{dp}$  ( $^\circ \text{ km}^{-1}$ ), the mean Doppler velocity ( $\text{m s}^{-1}$ ) and the Doppler spectral width  $SW$  ( $\text{m s}^{-1}$ ). During the FFT scans the full Doppler spectrum at  $0.17 \text{ m s}^{-1}$  resolution was retrieved. A semi-supervised hydrometeor classification (Besic et al., 2016) was applied on the polarimetric variables. A recently developed demixing module of this method (Besic et al., 2018) was also used to estimate the proportions of hydrometeor classes within one radar volume, which allows to study mixtures of hydrometeors.

### 2.2 W-band Doppler cloud profiler

WProf was deployed in MHS, 19 km inland of GWU at 789 m a.s.l. WProf is a frequency modulated continuous wave (FMCW) radar operating at 94 GHz, sampling the vertical column above the radar using typically three vertical chirps (Table

1). It consists of one transmitting and one receiving antenna. A comparison of MXPol and WProf specifications can be found in Table 2. WProf has an integrated passive radiometer at 89 GHz, which provides the brightness temperature of the vertical column above the radar (see Küchler et al., 2017 for more details).

### 2.3 Multi-angle snowflake camera

5 The MASC was deployed in a double fence wind shield in MHS. It is composed of three coplanar cameras separated by an angle of  $36^\circ$ . As hydrometeors fall in the triggering area, high resolution stereographic pictures are taken and their fall speed is measured. A complete description of the MASC can be found in Garrett et al. (2012). The MASC images were used as input parameters to a solid hydrometeor classification algorithm. Each individual particle is classified into six solid hydrometeor types, namely small particles (SP), columnar crystal (CC), planar crystal (PC), combination of column and plate crystal (CPC),  
10 aggregate (AG) and graupel (GR). In addition, the maximum dimension (diameter of the circumscribed circle) of particles is measured to characterise the size of the snowflakes. A detailed explanation of the algorithm is provided in Praz et al. (2017). One challenge during measurements of snowflakes in free-fall is the contamination from blowing snow. Schaer et al. (2018) developed a method to automatically identify blowing snow particles in MASC images. Despite the presence of a double fence wind shield during ICE-POP 2018, 31 % of the particles were identified as blowing snow and removed for this study. We will  
15 make use of particle size distributions estimated from the maximum diameter of particles following the work of Jullien et al. (2019).

### 2.4 Warm conveyor belt trajectory computation

We define the large-scale WCB ascent over the Korean peninsula in a Lagrangian perspective as a coherent ensemble of trajectories with an ascent rate of at least 600 hPa in 48 h (Wernli and Davies, 1997; Madonna et al., 2014). The 48-h trajectories  
20 were computed with the Lagrangian analysis tool LAGRANTO (Wernli and Davies, 1997; Sprenger and Wernli, 2015) based on the 1-hourly 3D wind field of the hydrostatic model IFS (model version Cy43r3 operational from July 2017 to June 2018, ECMWF 2017). The details of the microphysics scheme can be found in Forbes et al. (2011). The IFS is run with a spatial resolution of O1280 (approximately 9 km) and 137 vertical hybrid pressure-sigma levels (ECMWF, 2017). The IFS dataset combines operational analyses at 00:00, 06:00, 12:00 and 18:00 UTC with hourly short-term forecasts in between. The dataset  
25 was interpolated to a latitude/longitude grid with  $0.5^\circ$  spatial resolution for trajectory computation. To analyse the air parcel ascent in the vicinity of the measurement site, we combine 24-h backward and 24-h forward trajectories starting every hour between 00:00 UTC 27 February and 00:00 UTC 01 March 2018 every 50 hPa from 1000 hPa to 200 hPa in proximity of Pyeongchang. WCB trajectories are subsequently selected as trajectories exceeding an ascent rate of 600 hPa in 48 h. In addition to this Lagrangian representation (i.e. following the trajectories), we projected the WCB trajectories in an Eulerian  
30 reference frame above PyeongChang. This gives, for each time steps and for all vertical levels, the position of trajectories above PyeongChang which ascended with ascent rates of at least 600 hPa in 48 h within the period 00:00 UTC 27 February and 00:00 UTC 01 March 2018. This highlights at which heights WCB air parcels (i.e. with strong ascent at any given time) occur.

### 3 Synoptic overview and WCB

The 28 February 2018 precipitation event is the most intense of the whole ICE-POP 2018 campaign. It contributed 77 % of the winter 2018 (December–February) precipitation accumulation. At 18:00 UTC 27 February 2018 (Fig. 2a) a PV streamer (equatorwards excursion of stratospheric air) was located over eastern China and moved eastward towards South Korea. At 00:00 UTC 28 February 2018, (Fig. 2b) a surface cyclone has formed in the Yellow Sea east of the upper-level PV streamer. Towards 06:00 UTC, the surface cyclone intensified as the PV streamer was approaching (Fig. 2c) and became fully developed with a cold front passing to the south of the Korean peninsula and a warm front passing over Pyeongchang. The interaction between the upper-level PV streamer and the surface cyclone led to a rapid deepening of the cyclone by 25 hPa between 18:00 UTC 27 February and 12:00 UTC 28 February. The integrated vapour transport (IVT, Rutz et al., 2014) contours show the strong moisture flux ahead of the cold front with the most intense precipitation close to the cyclone center, where the IVT gradient is the largest. At 12:00 UTC the cyclone moved further east and the PV streamer was located over Korea inducing an increasingly easterly flow (Fig. 2d). While the Yellow Sea is a known region of cyclogenesis, the cyclone frequency over Korea in winter is less than 2 % (Wernli and Schwerz, 2006), indicating that such a synoptic situation in winter over Korea is relatively rare.

This intense precipitation event is associated with a WCB that ascends from the boundary layer to the upper troposphere and rises over the Korean peninsula during 28 February when the low pressure system was fully developed. Figure 3 shows an ensemble of trajectories that are part of the large-scale WCB airstream and that ascended near Pyeongchang at 06:00 UTC 28 February 2018. The inflow part of the WCB (i.e. upstream of the strong ascent in Fig. 3a) is characterised by IVT values greater than  $1000 \text{ kg m}^{-1} \text{ s}^{-1}$ , showing that the WCB transports large amounts of water vapour originating from the Yellow Sea. The trajectories are rapidly ascending over South Korea and liquid water content (LWC) increases along the selected WCB trajectories to above  $0.2 \text{ g kg}^{-1}$  in the region of strong ascent (Fig. 3b). The WCB ascent in the vicinity of the measurement site is relatively fast with ascent rates of approximately 500 hPa in 12 h (Fig. 4). During the relatively strong ascent from the boundary layer to the upper troposphere an extended mostly stratiform cloud band formed, which was also responsible for the surface precipitation (Fig. 5a,e). The WCB transported and formed up to  $0.20 \text{ g kg}^{-1}$  of liquid water during its strong ascent in the mid-troposphere (Figs. 3b and 4). The  $0^\circ \text{C}$  isotherm was higher than 900 hPa during the event. LWC increases along the ascent of the WCB trajectories above 900 hPa (Fig. 4). The increase in LWC in supercooled conditions is likely a result of (i) condensation on the water droplets advected from below to above freezing level and (ii) nucleation of new droplets at subfreezing temperatures. To maintain mixed-phase conditions, the depletion of liquid water by the Wegener–Bergeron–Findeisen process has to be compensated by production of liquid water by dynamical processes (e.g. advection of water droplets or condensation/nucleation in ascending air masses). Following this criteria, Heymsfield (1977) showed that for an ascending motion to maintain liquid water, the velocity of ascent has to be greater than a critical vertical velocity. We found that in this event a vertical velocity greater than  $0.1 \text{ m s}^{-1}$  would form supercooled droplets in the presence of both ice and snow particles (see Appendix A for details of the computation). The ascent rate of the WCB can be estimated from Fig. 4 to  $0.2 \text{ m s}^{-1}$ . We conclude that the simulated SLW is a consequence of the strong large-scale ascent in the WCB.

#### 4 The evolution of clouds and precipitation over Pyeongchang

In the previous section, we identified SLW associated with large-scale WCB ascents in IFS analyses. In the following, we use remote and in situ observations to corroborate the presence of SLW and to discuss its relevance for the microphysical processes taking place.

5 Before the onset of precipitation, a temperature inversion at 1500 m (Fig. 6a at 00:00 UTC) favours the formation of a low-level cloud (Fig. 5a). This temperature inversion is located just above a layer of potential instability with equivalent potential temperature ( $\theta_e$ ) gradients of about  $-10 \text{ K km}^{-1}$  between 1250 and 1450 m. Other layers of potential instability are present below 3000 m (with  $\theta_e$ -gradients up to  $-5 \text{ K km}^{-1}$ ) for all three radiosoundings at 00:00, 06:00 and 09:00 UTC. Above 3000 m, the air is saturated or close to saturation with respect to ice (Fig. 6b at 0000 UTC). At 06:00 and 09:00 UTC, the air is  
10 saturated with respect to ice over almost the entire troposphere. Between 6000 and 9000 m, the relative humidity with respect to ice (RH<sub>i</sub>) is well above saturation at 00:00, 06:00 and 09:00 UTC. This altitude range corresponds to the outflow of WCB air-masses (Fig. 4), which often features cirrus clouds (Madonna et al., 2014). These cirrus in the WCB outflow are likely composed of both ice crystals formed by freezing of liquid droplets in the WCB ascent and ice crystals formed via nucleation directly from the vapour phase in upper tropospheric air masses pushed upwards by the WCB (Wernli et al., 2016). This  
15 suggests that the high supersaturation with respect to ice above 6000 m is directly related to the WCB. In this view, the WCB provides favourable conditions for rapid crystal growth leading to precipitation onset. The profile of wind speed clearly shows a strong jet of  $45 \text{ m s}^{-1}$  at 6500 m a.s.l. at 06:00 UTC (Fig. 6c), which coincides with the WCB air masses. The height of this jet and the lower limit of WCB air masses decrease with time and we observe the jet just below 5000 m at 09:00 UTC. In the layer from 4000 to 6000 m a.s.l. at 06:00 UTC an increase of wind speed with height and a rapid change of the wind  
20 direction from southerly to south-westerly result in strong vertical wind shear. The vertical wind shear reaches values of  $15 \text{ m s}^{-1} \text{ km}^{-1}$  in speed and  $0.27^\circ \text{ m}^{-1}$  in direction. Keppas et al. (2018) identified similar values of vertical wind shear, which triggered Kelvin-Helmholtz instabilities. In Sect. 5.3, we illustrate the influence of this vertical wind shear within the WCB ascent region on the observed microphysics.

Figure 5a shows the reflectivity measured by WProf. The nimbostratus cloud is approaching between 00:00 and 03:00 UTC.  
25 The cloud base is at 3100 m (Fig. 6b), but virgas appear down to 2000 m where ice crystals sublime in unsaturated air. Below the temperature inversion at 1400 m the air is close to saturation (Fig. 6a,b at 00:00 UTC) and a low level cloud can be identified as a layer with reflectivity values below  $-5 \text{ dBZ}$ . At 03:00 UTC surface precipitation starts and lasts until 16:00 UTC (Fig. 5e). A 3D gridding of the WCB trajectory positions (Fig. 5,a,b black contour) reveals that WCB air parcels are continuously ascending above the location of WProf during the entire passage of the nimbostratus cloud. At 19:00 UTC a  
30 post-frontal precipitating system sets in and lasts until 00:00 UTC 01 March. It is not associated with the WCB and will not be investigated.

Within the WCB ascent regions, enhanced updraughts are present, in particular around 3000 m a.s.l. between 07:00 and 10:00 UTC (Fig. 5b). These overturning cells at the lower boundary of the WCB (represented by the black contour) are likely Kelvin-Helmholtz instabilities generated by the strong vertical wind shear observed in the radiosoundings (Fig. 6). Except for

a moist neutral layer around 4000 m at 06:00 UTC, the profiles at 06:00 and 09:00 have a stable lapse rate, which together with a strong wind shear provide favourable conditions for Kelvin-Helmholtz instabilities. A region of enhanced positive Doppler velocity can be observed from 07:30 to 08:00 UTC between 4000 and 6000 m where the mean Doppler velocity amounts to approximately  $2 \text{ m s}^{-1}$ , indicating the presence of embedded updraughts in the WCB. Recently, case studies by Keppas et al. (2018), Oertel et al. (2019a) and Oertel et al. (2019b) identified embedded convection within the large-scale WCB. Oertel et al. (2019a) and Oertel et al. (2019b) showed that embedded convection leads to a local increase in precipitation intensity, while Oertel et al. (2019b) found that it also promotes the formation of graupel particles in the model simulations. Finally, Hogan et al. (2002) observed that embedded convection was collocated with maxima of SLW concentration. In this paper we will refer to these upwards air motions as embedded updraughts, since there is no evidence of convective instability in the radiosoundings (Fig. 6a). While the cause of the updraughts we observe might be different than those mentioned in Hogan et al. (2002); Keppas et al. (2018); Oertel et al. (2019a), the consequence on precipitation growth processes is consistent with what we observe in this study.

Ahead of the precipitating system the cloud contains mainly crystals (Fig. 5c). Starting from 04:30 UTC the intense precipitation begins and aggregates dominate during the whole precipitation period. Rimed particles are also present, especially between 06:00 and 08:00 UTC when the proportion and vertical extent of rimed particles are the largest.

The brightness temperature measured by the radiometer (Fig. 5d) is the primary variable used to estimate the liquid water path (e.g. K  chler et al. 2017). In this study, we will use the brightness temperature as an indicator of the temporal evolution of the total liquid water in the atmospheric column. The maxima of brightness temperature observed when precipitation starts just before 04:00 UTC and the peak at 06:00 UTC corresponding to the local maximum of precipitation rate (Fig. 5e), are probably due to the partial melting of hydrometeors, since the temperature at MHS is above  $0^\circ\text{C}$ . The multiple peaks after 07:00 UTC (temperature drops below freezing), which are co-occurring with updraughts, suggest that the updraughts favour the production of SLW in addition to the SLW produced by the large-scale ascent in the WCB. There was unfortunately no CALIPSO (satellite onboard lidar) overpass to ascertain the presence of SLW during the event. There is a local maximum in the precipitation rate just after 06:00 UTC both at MHS and GWU (Fig. 5e), while the absolute maximum is about  $12 \text{ mm h}^{-1}$  at 09:40 UTC in MHS and  $13 \text{ mm h}^{-1}$  at 14:25 UTC in GWU. Except for the maximum at 14:25 UTC in GWU and the fact that precipitation occurred from 20:00 to 23:59 UTC in MHS but not in GWU, the temporal evolution of precipitation at both locations is very similar. Note that the surface warm front never reached Pyeongchang (only the precipitation associated with it), but moved further to the east. Hence, the surface temperature did not increase, in contrast to the temperature in the mid-troposphere, which increased by approximately 5 to  $10^\circ\text{C}$  (Fig. 6a) during the event.

## 5 Microphysical analysis of periods of interest

In the previous section we analysed the evolution of the dynamics and microphysics of the nimbostratus and precipitation associated with the warm front. In this section, we will analyse succeeding periods that reveal the link between the temporal evolution of the WCB and the microphysics over Pyeongchang. Based on the homogeneity of the dominant microphysical

processes, three different periods were selected: we first investigate the period dominated by depositional growth of crystals (Sect. 5.1) and subsequently analyse the effect of embedded updraughts on aggregation and riming (Sect. 5.2). Finally, we consider the impact of vertical wind shear and turbulence on aggregation (Sect. 5.3).

### 5.1 Vapour deposition: 03:00 to 04:00 UTC

- 5 The period from 03:00 to 04:00 UTC is dominated by crystals above 2000 m (Fig. 5c). At this time Pyeongchang is located ahead of the warm front. The vertical profiles of polarimetric variables (Fig. 7) show an increase of  $Z_H$  of 2 dBZ from 6000 m to 2000 m, while  $Z_{DR}$  is almost constant from 6000 m to 3000 m, and then subsequently decreases slightly. This likely indicates the onset of aggregation at 3000 m, below which temperatures are greater than  $-10\text{ }^{\circ}\text{C}$  and hence represent favourable conditions for aggregation (Hobbs et al., 1974).  $K_{dp}$  values are almost zero, suggesting that the number concentration of oblate crystals is low. In summary, this period is characterised by the presence of crystals in limited concentration, which grew by vapour deposition and likely aggregated below 3000 m.

- The selection of snowflake images (Fig. 8b, collected at an average temperature of  $1.5\text{ }^{\circ}\text{C}$ ) mainly shows small aggregates and crystals of about 2 mm in their maximum dimension. They are partly melted (liquid water is less reflective than ice and creates the dark areas on the snowflake pictures) and riming is indicated by the brighter areas. The size distribution shows that most particles are below 5 mm in size with a median of 2.2 mm. The classification shows that 64 % of the observed hydrometeors are aggregates, while above 2000 m, the MXPOL hydrometeor classification shows predominantly ice crystals (Fig 5c). This supports our previous conclusion that below 3000 m, when temperature increases and aggregation is more efficient, a large fraction of crystals aggregate. 7 % of particles were identified as graupel (Fig. 8b), which we could confirm by a visual analysis. Again the riming could have taken place below 2000 m, which explains why no rimed particles are present from 03:00 to 04:00 UTC in the MXPOL hydrometeor classification of Fig. 5c. Figure 9a shows the distribution of the riming index (0=no riming, 1=graupel, Praz et al. 2017). The mode around one corresponds to the graupel particles, while half of the particles had a riming index smaller than 0.4. This shows that except for the few graupel particles, the other hydrometeor classes did not feature significant riming in comparison with other periods of the event.

### 5.2 Embedded updraughts, riming and aggregation: 06:00 to 08:00 UTC

- 25 The period from 06:00 to 08:00 UTC is characterised by embedded updraughts (Fig. 5b), a layer with strong vertical wind shear at 3800 m (Figs. 6c,d) and significant riming, as seen by MXPOL (Fig. 5c). From 6000 m to 4800 m the crystals are growing by vapour deposition leading to an increase in both  $Z_H$  and  $Z_{DR}$  (Fig. 10) as particles grow mainly along their longest dimension leading to larger and more oblate crystals (Schneebeil et al., 2013; Andrić et al., 2013; Grazioli et al., 2015). The median of  $K_{dp}$  increases to only  $0.4\text{ }^{\circ}\text{km}^{-1}$ , suggesting that the number concentration of oblate particles is small. Temperature in this layer varies from  $-23\text{ }^{\circ}\text{C}$  to  $-16\text{ }^{\circ}\text{C}$  and the air is slightly above saturation with respect to ice (Fig. 6a,b). This represents favourable conditions for depositional growth of sectorial plates (Lohmann et al., 2016, Fig. 8.15), while aggregation is unlikely to dominate within this temperature range according to Hobbs et al. (1974). However, we can not rule out the formation of early aggregates, which at this stage would be oblate, and hence contribute to the increase in  $Z_{DR}$  (Moisseev et al., 2015).

At 4800 m we observe a peak and subsequent decrease in  $Z_{DR}$ , which marks the end of growth dominated by vapour deposition. We hypothesise that aggregation starts at this altitude. First, after aggregation snowflakes tend to be less oblate and less dense, which explains the decrease in  $Z_{DR}$ . Second, aggregation increases the size of snowflakes, and hence  $Z_H$  continues to increase.

- 5 The observed increase in  $K_{dp}$  below the peak in  $Z_{DR}$  is a commonly observed, but not fully understood feature. Andrić et al. (2013) proposed that secondary ice generation of small oblate crystals could explain the observed enhanced  $K_{dp}$  values. Concentration of secondary ice particles can be much larger than the number of snowflakes they originate from, which would affect  $K_{dp}$  more strongly than  $Z_{DR}$  since the former is more sensitive to concentration. Moisseev et al. (2015) suggested that it is the result of the onset of aggregation, producing early aggregates that are relatively oblate. Our hypothesis is that first,
- 10 the generation of secondary ice by droplet shattering (Mason and Maybank, 1960) and ice-ice collisions (Vardiman, 1978; Takahashi et al., 1995; Yano and Phillips, 2011) contributes to the increase in  $K_{dp}$  below 5000 m a.s.l. Droplet shattering shows a maximum of occurrence at  $-17\text{ }^{\circ}\text{C}$  (Leisner et al., 2014), which corresponds to the altitude where LWC is converted into IWC (Fig. 4 around 5000 m asl). Secondary ice generation by ice-ice collision is most effective at  $-15\text{ }^{\circ}\text{C}$  (Takahashi, 1993) and may also take place at around 5000 m a.s.l. Second, riming of already oblate crystals will tend to increase  $K_{dp}$ , because
- 15 in the early stage of riming the cavities in the crystals are filled, increasing the density (and thus the dielectric response) of the hydrometeors without changing their aspect ratio. Third, rime splintering by the Hallett-Mossop process (Hallett and Mossop, 1974) below 2500 m a.s.l. (temperature above  $-8\text{ }^{\circ}\text{C}$ ) can contribute to maintain high  $K_{dp}$  values. Finally, Korolev et al. (2019) recently suggested that secondary ice produced by shattering of freezing droplets transported above the melting layer could be lifted to higher levels. This may enhance the concentration of secondary ice in regions of strong updraughts. Note that the
- 20 higher  $K_{dp}$  values compared to the period 03:00–04:00 UTC is primarily due to the increase of precipitation intensity, but the fact that  $K_{dp}$  increases below the onset of aggregation cannot be explained by precipitation intensity only, since aggregation decreases the number concentration and the oblateness of the particles. Riming will initially increase  $K_{dp}$  by first filling cavities and hence increasing the density of particles, but will later lead to a decrease in  $K_{dp}$  as the rime mass will smooth the particles' shape. There has to be a mechanism which produces a high number concentration of oblate particles to explain an increase in
- 25  $K_{dp}$  in a layer dominated by aggregation and riming and secondary ice production is a good candidate.

- At 3800 m a strong vertical wind shear in the lower part of the WCB (black contour in Fig. 5a,b,c at 06:00 UTC) can be observed in both the radiosoundings (Fig. 6c,d) and the spectral width profiles (Fig. 10). The jet at 6500 m at 06:00 UTC (Fig. 6c) can be seen as an enhancement of Doppler velocity between 4000 and 6000 m a.s.l. with a maximum of  $45\text{ m s}^{-1}$  at 5000 m in the RHI of Fig. 11. This is in good agreement with the wind speed measured by the radiosonde at 06:00 UTC, since the
- 30 RHI is almost aligned with the wind direction. The vertical wind shear at 3800 m is visible as the Doppler velocity decreases in the lower part of the WCB and reaches a value of  $0\text{ m s}^{-1}$  at 3000 m (combined effect of a decrease in wind speed and change of wind direction from parallel to perpendicular to the radar beam). This vertical wind shear may generate Kelvin-Helmholtz instabilities, which can trigger embedded convection (Hogan et al., 2002). Moreover orography might also play a role in lifting the easterly low-level flow, which directly impinges the Taebaek mountains from the East Sea. These sources of lifting together
- 35 with the moist neutral layers below 3000 m (Fig. 6a) can lead to the observed strong updraughts (Fig. 5b), which promote

aggregation by increasing the probability of collisions between particles. The effect of turbulent cells on aggregation has been discussed thoroughly in Houze and Medina (2005), Medina et al. (2005) and Medina and Houze (2015). Houze and Medina (2005) suggested that overturning cells promote both aggregation and riming. First, they can sustain the production of SLW necessary for riming. Second, the turbulence increases the probability of collision between particles. Finally, aggregates are larger targets for the collection of SLW droplets, which again enhances growth by riming. While the cause of the turbulence is different here, the processes described are consistent with our measurements.

The MASC images (Fig. 12a) show mainly rimed aggregates of about 10 mm in their maximum dimension and two graupel particles. The average temperature of collection was 0.1 °C and hence the particles should not be as melted as during the period 03:00–04:00 UTC. The classification shows a majority of aggregates (77 %). The hydrometeor classification from Besic et al. (2018) classifies rimed aggregates and graupel as rimed particles, whereas the MASC based classification from Praz et al. (2017) classifies only fully rimed particles as graupel and the aggregates class contains also rimed aggregates. Therefore a direct comparison of the class aggregates between the two classification methods is difficult. The size distribution is much broader than from 03:00 to 04:00 UTC with particles reaching 13 mm in their maximum dimension. The median amounts to 2.8 mm, as there is still a significant proportion of small particles. The total number of particles is 589, while it was 55 in the previous period, showing that this period features more intense precipitation, which also makes the empirical size distribution more robust. The 75th percentile is 4.7 mm compared to 3.0 mm for the period 03:00 to 04:00 UTC, showing that the particles from 06:00 to 08:00 UTC are significantly larger. These large rimed aggregates can be attributed to the strong updraughts, which enhance the growth by aggregation and riming. Note that while the previous period (Sec. 5.1) featured riming below 2000 m, the precipitation rate was much smaller than from 06:00 to 08:00 UTC (Fig. 5e) and hence this riming did not contribute significantly to the total precipitation accumulation. The important message here is that the flow conditions in the WCB promoted rapid precipitation growth by aggregation and riming above 2000 m and are thus responsible for the large precipitation accumulation between 06:00 to 08:00 UTC. Moreover, most of the particles have higher quartiles of riming index (Fig. 9b) than between 03:00 to 04:00 UTC, despite the lower proportion of graupels, which is due to the enhanced aggregation favouring rimed aggregates at the expense of pure graupel. We conclude that this period features the most riming, both in absolute mass and in relative terms over all hydrometeor classes.

Figure 13 shows a range spectrogram from WProf averaged from 07:42 UTC to 07:47 UTC and from 07:57 UTC to 08:02 UTC. The updraught present in Fig. 5b can be seen as a strong shift in the mode of the spectrum from about  $-0.5 \text{ m s}^{-1}$  at 6000 m to above  $2 \text{ m s}^{-1}$  at 5000 m (Fig. 13a). This updraught goes along with strong turbulence which is visible as an increase in spectral width between 4000 m and 6000 m. By 07:57 UTC (Fig. 13b), the increase in spectral reflectivity together with a decrease in Doppler velocity from 4800 to 4000 m suggests that large aggregates likely formed in the turbulent layer and further aggregate during their fall. This is consistent with the onset of aggregation below 5000 m observed in Fig. 10. The enhanced aggregation in the updraughts present from around 07:30 UTC to 08:00 UTC leads to an increase of precipitation rate from 07:55 UTC to the maximum at 09:40 UTC (Fig. 5e). Particles that started falling between 4000 and 5000 m will take 85–105 min to fall to the ground with an average effective fall speed (absolute fall speed plus updraught) of  $0.8 \text{ m s}^{-1}$ . This is consistent with the increase in precipitation intensity from 07:55 to 09:40 UTC and the maximum could correspond to aggregates that

formed in the updraught between 07:35 to 07:55 UTC. This hypothesis assumes a certain horizontal homogeneity, supported by the increase in precipitation in both rain gauge measurements in MHS and GWU that are separated by 19 km (Fig. 5e). It would imply that the embedded updraughts are responsible for the period of strongest precipitation, which also features intense riming (Fig. 5c), consistent with the suggestion in Oertel et al. (2019a, b).

### 5 5.3 Shear-induced turbulence: 09:00 to 11:00 UTC

The period from 09:00 to 11:00 UTC features turbulence and intense precipitation rates (Fig. 5b, e). Due to a malfunction of the MASC, only pictures between 10:08 and 10:50 UTC were collected, leading to only 69 particles during this period (Fig. 14). There are substantially more crystals (10 %) than during the other periods. Figure 14a shows a few small aggregates, columnar and planar crystals and one graupel. The median of the size distribution is at 2.7 mm, and the 75th and 95th percentiles are at 3.9 mm and 6.6 mm, respectively, indicating that the particles are smaller than in the previous period. Figure 15 shows a less pronounced increase in  $Z_{DR}$  compared to the period between 06:00 to 08:00 UTC (Fig. 10), suggesting that the depositional growth rate is smaller than during the previous period. The median of  $Z_{DR}$  increases to 0.7 dB around 4200 m, where crystals and aggregates probably dominate. The median of  $Z_H$  reaches a maximum of 22 dBZ at 2000 m, compared to 25 dBZ at 06:00–08:00 UTC (Fig. 10). This is consistent with the size distribution (06:00–08:00 UTC in Fig. 12) that shows more large particles than Fig. 14. Below 4200 m, larger aggregates start to form as temperatures exceed  $-15\text{ }^{\circ}\text{C}$  and  $Z_{DR}$  decreases slightly. It is collocated with the increase in spectral width (Fig. 15), reflecting the vertical wind shear below the maximum wind speed (6c) at 09:00 UTC. The shear layer was between 4000 and 5000 m in the period from 06:00 to 08:00 UTC, while it is now between 3000 m and 4000 m. This vertical wind shear is collocated with the turbulent cells observed in Fig. 5b from 08:00 to 10:00 UTC around 4000 m, which suggests that they originate from Kelvin-Helmholtz instabilities. This is supported by values of the gradient Richardson number (not shown here) of 0.2 where the turbulent cells are present. The decrease in the height of the wind shear is consistent with the decrease in the height of maximum wind speed between 06:00 and 09:00 UTC (Fig. 6c), and explains why the altitude of aggregation enhancement by turbulence decreases with time. This was also observed by Keppas et al. (2018), who attributed this altitude decrease of the maximum of wind speed to the passage of the warm front. On the other hand, the altitude of the onset of aggregation could increase with time as the warm front passes, because the altitude of the  $-15\text{ }^{\circ}\text{C}$  isotherm [relative maximum of aggregation in Hobbs et al., 1974] is higher at 09:00 UTC than at 06:00 UTC. Our interpretation is that the enhancement of aggregation by turbulence dominates the polarimetric signatures in our case. First, because crystals were likely growing as sectorial plates and not as dendrites, the latter being more effective to aggregate at  $-15\text{ }^{\circ}\text{C}$ . Second, the intense aggregation taking place in the shear layer leads to larger aggregates than the early aggregation at  $-15\text{ }^{\circ}\text{C}$ , which makes the former more visible in the polarimetric profiles. The distribution of the riming index (Fig. 9c) is broader than for the other periods due to the higher proportions of crystal-like particles and the presence of graupel and rimed aggregates.

## 6 A conceptual model

The findings of this case study can be summarised in a conceptual model (Fig. 16). As the WCB rises from the boundary layer, the air saturates and the liquid water droplets eventually become supercooled. If the ascent rate is strong enough (which is the case for most WCBs, see Sect. 3), SLW can be produced and persist to the mid-troposphere. Crystals grow by vapour deposition at upper levels of the WCB ascent (see  $RH_i > 110\%$  in Fig. 6b) leading to an increase in  $Z_H$  and  $Z_{DR}$ . During their fall, they experience riming by accretion of supercooled droplets. Moreover, the vertical wind shear (large  $SW$ ) at the lower-boundary of the WCB creates turbulence, which enhances aggregation by increasing the probability of collisions between hydrometeors. Furthermore, embedded updraughts in the WCB (as seen by positive vertical Doppler velocities) can additionally lift precipitating particles and increases their time for growth by aggregation. Finally, aggregates are larger targets for collection of SLW, which enhances riming. This leads to large rimed aggregates and local peaks in precipitation intensity. In the layer of growth by aggregation and riming,  $Z_H$  increases, while  $Z_{DR}$  decreases. Additionally, generation of secondary ice by droplet shattering and ice-ice collision leads to an increase in  $K_{dp}$ . In the outflow region of the WCB, crystals, which either formed by nucleation from the vapour phase or freezing of the remaining supercooled droplets, fall and may aggregate without significant riming. While this conceptual model is built upon a single case study, we postulate that the key processes, which are production of SLW and turbulence enhancing riming and aggregation, can take place in most wintertime mid-latitude cyclones featuring a strong WCB.

## 7 Conclusion

This study investigates the snowfall microphysics associated with a WCB during an extreme wintertime precipitation event in South Korea. We combined Doppler dual-polarisation radar measurements, snowflake photographs, radiosonde data with IFS data and trajectories to characterise the detailed precipitation growth mechanisms associated with the large-scale WCB ascent.

The main findings can be summarised as follows:

- We identified a WCB in IFS analyses as rapidly ascending air masses (approximately 600 hPa in 12 h) in the vicinity of Pyeongchang. A strong jet and enhanced vertical wind shear within the WCB ascent region are clearly visible in radiosonde data and Doppler velocity measurements from MXPOL.
- The IFS analyses show that SLW (up to  $0.2 \text{ g kg}^{-1}$ ) is produced during the rapid ascent in the WCB by condensation of water vapour. In agreement with IFS analyses, multiple peaks in the brightness temperature of the radiometer during the passage of the warm front corroborate the presence of SLW. The timing and presence of SLW is additionally confirmed by the presence of rimed particles observed by the MASC and a hydrometeor classification based on MXPOL data.
- The vertical wind shear promotes aggregation and riming by producing SLW, updraughts and turbulence, which enhance the probability of collisions between particles.

- Three periods could be identified, where the governing microphysical processes are directly influenced by the specific flow conditions in the WCB. In the first period, Pyeongchang is located below the WCB outflow (Fig. 5a). No strong updraughts were present, the precipitation intensity was low and we observed mainly small aggregates and crystals. In the second and third periods, Pyeongchang is located below WCB ascent. A layer with strong vertical wind shear, whose height decreases with time, generates turbulent cells and updraughts. The precipitation intensity peaks between 7 and 10 mm h<sup>-1</sup> and large rimed aggregates are observed.

This study enabled the investigation of the impact of a large-scale feature, such as a WCB, on the microphysics thanks to the complementarity of atmospheric models, remote-sensing and in situ measurements. It suggests a strong coupling between processes on the synoptic and micro-scales that has to be assessed when evaluating the representation of cloud and precipitation in atmospheric models. While this case study presents a detailed analysis of field measurements, additional investigations with in situ measurements in clouds - characterising the presence of SLW for instance - are needed to further constrain and evaluate the coupling between large-scale dynamical processes and microphysics in models.

*Code and data availability.* The trajectories were computed with the Lagrangian analysis tool LAGRANTO (Sprenger and Wernli, 2015). We used functions from the Python libraries Py-ART (Helmus and Collis, 2016) and MetPy (May et al., 2008). Other codes and data are available upon request to the corresponding author.

## Appendix A: Estimation of the critical vertical velocity

In this appendix we will show details on the estimation of the critical vertical velocity  $U_z^*$  needed to form and maintain liquid water in the presence of both ice crystals and snow. Korolev and Mazin (2003) showed that  $U_z^*$  can be expressed as a function of pressure, temperature, number concentration and mean size of ice crystals. We use Fig. 10 in Korolev and Mazin (2003), which gives the relation between  $U_z^*$  and the product of the number concentration of ice particles  $N_i$  and the characteristic size of ice particles  $r_i$  for temperature between -35°C and -5°C. Since in our case we have both ice and snow particles, we compute separately  $N_i$  and the number concentration of snow particles  $N_s$  such that the total number concentration is:  $N_{tot} = N_i + N_s$ . We also compute the characteristic size of the mixture of ice and snow particles  $r_{tot}$ . The expression for  $N_i$  is given by Eq. 7.40 of ECMWF (2016):

$$N_i = 100 \exp[12.96(e_{sl} - e_{si})/e_{si} - 0.639], \quad (A1)$$

where  $e_{sl}$  ( $e_{si}$ ) is the saturation vapour pressure with respect to liquid (ice). The expression for  $N_s$  is given by Eqs. 7.15 to 7.19 in ECMWF (2016). In our case it is simply expressed by:

$$N_s = \Lambda^{-1} N_{0s}, \quad (A2)$$

where  $N_{0s} = n_{as} = 2 \cdot 10^6$  (Eq. 7.16 and Table 7.1 of ECMWF (2016)) and  $\Lambda$  is given by (Eq. 7.18 of ECMWF 2016):

$$\Lambda = \left( \frac{n_{as} a_s \Gamma(3)}{q_s \rho_s} \right)^{1/(b_s+1-n_{bs})} \quad (\text{A3})$$

$$\Gamma(3) = \int_0^\infty D^2 e^{-D} dD = 2, \quad (\text{A4})$$

where  $a_s = 0.069$ ,  $b_s = 2$ ,  $n_{bs} = 0$  are given in Table 7.1 and 7.2 of ECMWF (2016). The expression for  $r_i$  can be found by

5 stating that the characteristic volume of an ice particle  $V_i$  is:

$$V_i = \frac{\rho q_i}{\rho_i N_i}, \quad (\text{A5})$$

where  $\rho$  is the air density,  $\rho_i$  the density of ice particles and  $q_i$  the mixing ratio of ice. Assuming spherical particles, we can express  $r_i$  with:

$$r_i = \left( \frac{3 \rho q_i}{4 \rho_i N_i \pi} \right)^{1/3}, \quad (\text{A6})$$

10 Since snow particles are spherical in IFS and considered as having the same density as ice, we have  $\rho_i = \rho_s$ . We define  $r_{tot}$  as:

$$r_{tot} = \left( \frac{3 \rho (q_i + q_s)}{4 \rho_i N_{tot} \pi} \right)^{1/3} \quad (\text{A7})$$

Using the values described in Table A1, we find  $N_{tot} r_{tot} = 1.7 \mu\text{m cm}^{-3}$ , which we can use in Fig. 10 of Korolev and Mazin (2003) to read  $U_z^*$  at about  $-13^\circ\text{C}$  and find  $0.1 \text{ m s}^{-1}$ .

15 *Author contributions.* JG and AB designed the experiment. JG operated the instruments, processed and analysed the observational data. AO computed and analysed the WCB trajectories. NJ computed the MASC size distributions. NB computed the radar based hydrometeor classification. JG, AO, EV and AB interpreted the data. JG, with contributions of all authors, prepared the manuscript.

*Competing interests.* The authors declare that they have no conflict of interest.

*Acknowledgements.* We are grateful for the support provided by the Korea Meteorological Administration and the World Meteorological  
20 Organisation making possible the ICE-POP 2018 weather research and development projects and the observational data used in this publication. In particular, we are thankful to the High Impact Weather Research Center of the Korea Meteorological Organisation for providing

us with radiosonde data and giving us access to their facilities at the Gangneung Wonju National University. We would also like to thank Christophe Praz and Jacques Grandjean for their help during the deployment of the instruments. Special thanks go to KwangDeuk Ahn from the Korea Meteorological Organisation for his support during the campaign and to Kwonil Kim for his help with some instruments. Finally, we would like to thanks Hanna Joos and Heini Wernli from ETH for their review and constructive comments on the manuscript. JG and AO  
5 acknowledge the financial support from the Swiss National Science Foundation (grants 175700/1 and 165941, respectively).

## References

- Andrić, J., Kumjian, M. R., Zrnić, D. S., Straka, J. M., and Melnikov, V. M.: Polarimetric signatures above the melting layer in winter storms: An observational and modeling study, *Journal of Applied Meteorology and Climatology*, 52, 682–700, <https://doi.org/10.1175/JAMC-D-12-028.1>, 2013.
- 5 Bader, M. J., Clough, S. A., and Cox, G. P.: Aircraft and dual polarization radar observations of hydrometeors in light stratiform precipitation, *Quarterly Journal of the Royal Meteorological Society*, 113, 491–515, <https://doi.org/10.1002/qj.49711347605>, 1987.
- Besic, N., Figueras i Ventura, J., Grazioli, J., Gabella, M., Germann, U., and Berne, A.: Hydrometeor classification through statistical clustering of polarimetric radar measurements: A semi-supervised approach, *Atmospheric Measurement Techniques*, 9, 4425–4445, <https://doi.org/10.5194/amt-9-4425-2016>, 2016.
- 10 Besic, N., Gehring, J., Praz, C., Figueras i Ventura, J., Grazioli, J., Gabella, M., Germann, U., and Berne, A.: Unraveling hydrometeor mixtures in polarimetric radar measurements, *Atmospheric Measurement Techniques*, 11, 4847–4866, <https://doi.org/10.5194/amt-11-4847-2018>, 2018.
- Bringi, V. N. and Chandrasekar, V.: *Polarimetric Doppler Weather Radar: Principles and Applications*, Cambridge University Press, <https://doi.org/10.1017/CBO9780511541094>, 2001.
- 15 Browning, K. A.: *Organisation of clouds and precipitation in extratropical cyclones*, Amer. Meteorol. Soc., Boston, MA, 1990.
- Browning, K. A., Hardman, M. E., Harrold, T. W., and Pardoe, C. W.: The structure of rainbands within a mid-latitude depression, *Quarterly Journal of the Royal Meteorological Society*, 99, 215–231, <https://doi.org/10.1002/qj.49709942002>, 1973.
- Carlson, T. N.: Airflow through midlatitude cyclones and the comma cloud pattern., [https://doi.org/10.1175/1520-0493\(1980\)108<1498:ATMCAT>2.0.CO;2](https://doi.org/10.1175/1520-0493(1980)108<1498:ATMCAT>2.0.CO;2), 1980.
- 20 Colle, B. a., Stark, D., and Yuter, S. E.: Surface Microphysical Observations within East Coast Winter Storms on Long Island, New York, *Monthly Weather Review*, 142, 3126–3146, <https://doi.org/10.1175/MWR-D-14-00035.1>, 2014.
- Dacre, H. F., Martínez-Alvarado, O., and Mbengue, C. O.: Linking Atmospheric Rivers and Warm Conveyor Belt Airflows, *Journal of Hydrometeorology*, 20, 1183–1196, <https://doi.org/10.1175/jhm-d-18-0175.1>, 2019.
- Eckhardt, S., Stohl, A., Wernli, H., James, P., Forster, C., and Spichtinger, N.: A 15-year climatology of warm conveyor belts, *Journal of Climate*, 17, 218–237, [https://doi.org/10.1175/1520-0442\(2004\)017<0218:AYCOWC>2.0.CO;2](https://doi.org/10.1175/1520-0442(2004)017<0218:AYCOWC>2.0.CO;2), 2004.
- 25 ECMWF: IFS Documentation – Cy41r2, Part IV: Physical Processes, <https://www.ecmwf.int/sites/default/files/elibrary/2016/16648-part-iv-physical-processes.pdf>, last access: 16 April 2020, 2016.
- ECMWF: IFS Documentation - Cy43r3: Operational implementation 11 July 2017. Dynamics and numerical procedures., 2017.
- Forbes, R., Tompkins, A., and Untch, A.: A new prognostic bulk microphysics scheme for the IFS, p. 22, <https://doi.org/10.21957/bf6vjvxxk>, <https://www.ecmwf.int/node/9441>, 2011.
- 30 Garrett, T. J., Fallgatter, C., Shkurko, K., and Howlett, D.: Fall speed measurement and high-resolution multi-angle photography of hydrometeors in free fall, *Atmospheric Measurement Techniques*, 5, 2625–2633, <https://doi.org/10.5194/amt-5-2625-2012>, 2012.
- Grazioli, J., Lloyd, G., Panziera, L., Hoyle, C. R., Connolly, P. J., Henneberger, J., and Berne, A.: Polarimetric radar and in situ observations of riming and snowfall microphysics during CLACE 2014, *Atmospheric Chemistry and Physics*, 15, 13 787–13 802, <https://doi.org/10.5194/acp-15-13787-2015>, 2015.
- 35 Green, J. S., Ludlam, F. H., and McIlveen, J. F.: Isentropic relative flow analysis and the parcel theory, *Quarterly Journal of the Royal Meteorological Society*, 92, 210–219, <https://doi.org/10.1002/qj.49709239204>, 1966.

- Hallett, J. and Mossop, S. C.: Production of secondary ice particles during the riming process, *Nature*, 249, 26–28, <https://doi.org/10.1038/249026a0>, 1974.
- Harrold, T.: Mechanisms influencing the distribution of precipitation within baroclinic disturbances, *Quarterly Journal of the Royal Meteorological Society*, 99, 232–251, 1973.
- 5 Hawcroft, M. K., Shaffrey, L. C., Hodges, K. I., and Dacre, H. F.: How much Northern Hemisphere precipitation is associated with extratropical cyclones?, *Geophysical Research Letters*, 39, 1–7, <https://doi.org/10.1029/2012GL053866>, 2012.
- Helmus, J. J. and Collis, S. M.: The Python ARM Radar Toolkit (Py-ART), a Library for Working with Weather Radar Data in the Python Programming Language, *Journal of Open Research Software*, 4, <https://doi.org/10.5334/jors.119>, 2016.
- Heymsfield, A. J.: Precipitation Development in Stratiform Ice Clouds: A Microphysical and Dynamical Study, [https://doi.org/10.1175/1520-0469\(1977\)034<0367:pdiscic>2.0.co;2](https://doi.org/10.1175/1520-0469(1977)034<0367:pdiscic>2.0.co;2), 1977.
- 10 Hobbs, P. V., Chang, S., and Locatelli, J. D.: The dimensions and aggregation of ice crystals in natural clouds, *Journal of Geophysical Research*, 79, 2199–2206, <https://doi.org/10.1029/JC079i015p02199>, <http://doi.wiley.com/10.1029/JC079i015p02199>, 1974.
- Hogan, R. J., Field, P. R., Illingworth, a. J., Cotton, R. J., and Choullarton, T. W.: Properties of embedded convection in warm-frontal mixed-phase cloud from aircraft and polarimetric radar, *Quarterly Journal of the Royal Meteorological Society*, 128, 451–476, <https://doi.org/10.1256/003590002321042054>, <http://dx.doi.org/10.1256/003590002321042054>, 2002.
- 15 Houze, R. a. and Medina, S.: Turbulence as a Mechanism for Orographic Precipitation Enhancement, *Journal of the Atmospheric Sciences*, 62, 3599–3623, <https://doi.org/10.1175/JAS3555.1>, 2005.
- Joos, H. and Forbes, R. M.: Impact of different IFS microphysics on a warm conveyor belt and the downstream flow evolution, *Q. J. Roy. Meteor. Soc.*, 142, 2727–2739, <https://doi.org/10.1002/qj.2863>, 2016.
- 20 Joos, H. and Wernli, H.: Influence of microphysical processes on the potential vorticity development in a warm conveyor belt: A case-study with the limited-area model COSMO, *Quarterly Journal of the Royal Meteorological Society*, 138, 407–418, <https://doi.org/10.1002/qj.934>, 2012.
- Jullien, N., Vignon, É., Reverdin, A., Praz, C., and Berne, A.: Snowfall particle size distributions at Dumont d’Urville station from MASC measurements, in: 27th IUGG Assembly, p. 1, Montréal, 2019.
- 25 Keppas, S. C., Crosier, J., Choullarton, T. W., and Bower, K. N.: Microphysical properties and radar polarimetric features within a warm front, *Monthly Weather Review*, 146, 2003–2022, <https://doi.org/10.1175/MWR-D-18-0056.1>, 2018.
- Korolev, A., Heckman, I., Wolde, M., Ackerman, A. S., Fridlind, A. M., Ladino, L., Lawson, P., Milbrandt, J., and Williams, E.: A new look at the environmental conditions favorable to secondary ice production, *Atmospheric Chemistry and Physics Discussions*, pp. 1–67, <https://doi.org/10.5194/acp-2019-611>, 2019.
- 30 Korolev, A. V. and Mazin, I. P.: Supersaturation of water vapor in clouds, *Journal of the Atmospheric Sciences*, 60, 2957–2974, [https://doi.org/10.1175/1520-0469\(2003\)060<2957:SOWVIC>2.0.CO;2](https://doi.org/10.1175/1520-0469(2003)060<2957:SOWVIC>2.0.CO;2), 2003.
- Küchler, N., Kneifel, S., Löhnert, U., Kollias, P., Czekala, H., and Rose, T.: A W-Band Radar–Radiometer System for Accurate and Continuous Monitoring of Clouds and Precipitation, *Journal of Atmospheric and Oceanic Technology*, 34, 2375–2392, <https://doi.org/10.1175/JTECH-D-17-0019.1>, <http://journals.ametsoc.org/doi/10.1175/JTECH-D-17-0019.1>, 2017.
- 35 Kumjian, M.: Principles and applications of dual-polarization weather radar. Part III: Artifacts, *Journal of Operational Meteorology*, 1, 265–274, <https://doi.org/10.15191/nwajom.2013.0121>, 2013.

- Kumjian, M. R., Rutledge, S. A., Rasmussen, R. M., Kennedy, P. C., and Dixon, M.: High-resolution polarimetric radar observations of snow-generating cells, *Journal of Applied Meteorology and Climatology*, 53, 1636–1658, <https://doi.org/10.1175/JAMC-D-13-0312.1>, 2014.
- Leisner, T., Pander, T., Handmann, P., and Kiselev, A.: Secondary ice processes upon heterogeneous freezing of cloud droplets, in: 14th Conf. on Cloud Physics and Atmospheric Radiation, edited by Amer. Meteor. Soc., .., Boston, MA, 2014.
- Lohmann, U., Luond, F., and Mahrt, F.: *An Introduction to Clouds*, Cambridge Univ. Press, 2016.
- Madonna, E., Wernli, H., Joos, H., and Martius, O.: Warm conveyor belts in the ERA-Interim Dataset (1979-2010). Part I: Climatology and potential vorticity evolution, *Journal of Climate*, 27, 3–26, <https://doi.org/10.1175/JCLI-D-12-00720.1>, 2014.
- Mason, B. J. and Maybank, J.: The fragmentation and electrification of freezing water drops, *Q. J. Roy. Meteor. Soc.*, 86, 176–185, [https://doi.org/10.1175/1520-0469\(1975\)032<0974:TFAEOF>2.0.CO;2](https://doi.org/10.1175/1520-0469(1975)032<0974:TFAEOF>2.0.CO;2), 1960.
- May, R. M., Arms, S. C., Marsh, P., Bruning, E., and Leeman, J. R.: MetPy: A Python package for meteorological data, <https://doi.org/10.5065/D6WW7G29>, <https://github.com/Unidata/MetPy>, 2008.
- Medina, S. and Houze, R. A.: Small-Scale Precipitation Elements in Midlatitude Cyclones Crossing the California Sierra Nevada, *Monthly Weather Review*, 143, 2842–2870, <https://doi.org/10.1175/MWR-D-14-00124.1>, <http://journals.ametsoc.org/doi/10.1175/MWR-D-14-00124.1>, 2015.
- Medina, S., Smull, B. F., Houze, R. A., and Steiner, M.: Cross-Barrier Flow during Orographic Precipitation Events: Results from MAP and IMPROVE, *Journal of the Atmospheric Sciences*, 62, 3580–3598, <https://doi.org/10.1175/jas3554.1>, 2005.
- Moisseev, D. N., Lautaportti, S., Tyynela, J., and Lim, S.: Dual-polarization radar signatures in snowstorms: Role of snowflake aggregation, *Journal of Geophysical Research: Atmospheres*, 120, 12 644–12 655, <https://doi.org/10.1002/2015JD023884>, 2015.
- Oertel, A., Boettcher, M., Joos, H., Sprenger, M., Konow, H., Hagen, M., and Wernli, H.: Convective activity in an extratropical cyclone and its warm conveyor belt – a case-study combining observations and a convection-permitting model simulation, *Quarterly Journal of the Royal Meteorological Society*, 145, 1406–1426, <https://doi.org/10.1002/qj.3500>, 2019a.
- Oertel, A., Boettcher, M., Joos, H., Sprenger, M., and Wernli, H.: Potential vorticity structure of embedded convection in a warm conveyor belt and its relevance for the large-scale dynamics, *Weather and Climate Dynamics Discussions*, pp. 1–38, <https://doi.org/10.5194/wcd-2019-3>, 2019b.
- Pfahl, S., Madonna, E., Boettcher, M., Joos, H., and Wernli, H.: Warm conveyor belts in the ERA-Interim data set (1979-2010). Part II: Moisture origin and relevance for precipitation, *Journal of Climate*, 27, 27–40, <https://doi.org/10.1175/JCLI-D-13-00223.1>, <http://journals.ametsoc.org/doi/abs/10.1175/JCLI-D-13-00223.1>, 2014.
- Praz, C., Roulet, Y.-A., and Berne, A.: Solid hydrometeor classification and riming degree estimation from pictures collected with a Multi-Angle Snowflake Camera, *Atmospheric Measurement Techniques*, pp. 1–40, <https://doi.org/10.5194/amt-2016-417>, <http://www.atmos-meas-tech-discuss.net/amt-2016-417/>, 2017.
- Rutz, J. J., James Steenburgh, W., and Martin Ralph, F.: Climatological characteristics of atmospheric rivers and their inland penetration over the western united states, *Monthly Weather Review*, 142, 905–921, <https://doi.org/10.1175/MWR-D-13-00168.1>, 2014.
- Schaer, M., Praz, C., and Berne, A.: Identification of blowing snow particles in images from a multi-angle snowflake camera, *The Cryosphere Discussions*, pp. 1–23, <https://doi.org/10.5194/tc-2018-248>, 2018.
- Schneebeli, M., Dawes, N., Lehning, M., and Berne, A.: High-resolution vertical profiles of X-band polarimetric radar observables during snowfall in the Swiss Alps, *Journal of Applied Meteorology and Climatology*, 52, 378–394, <https://doi.org/10.1175/JAMC-D-12-015.1>, 2013.

- Schultz, D. M.: Reexamining the cold conveyor belt, *Monthly Weather Review*, 129, 2205–2225, [https://doi.org/10.1175/1520-0493\(2001\)129<2205:RTCCB>2.0.CO;2](https://doi.org/10.1175/1520-0493(2001)129<2205:RTCCB>2.0.CO;2), 2001.
- Sprenger, M. and Wernli, H.: The LAGRANTO Lagrangian analysis tool - Version 2.0, *Geoscientific Model Development*, 8, 2569–2586, <https://doi.org/10.5194/gmd-8-2569-2015>, 2015.
- 5 Takahashi, T.: High ice crystal production in winter cumuli over the Japan Sea, *Geophysical Research Letters*, 20, 451–454, <https://doi.org/10.1029/93GL00613>, 1993.
- Takahashi, T., Yoshihiro Nagao, and Kushiya, Y.: Possible High Ice Particle Production during Graupel–Graupel Collisions, *American Meteorological Society*, 52, 4523–4527, 1995.
- Vardiman, L.: The Generation of Secondary Ice Particles in Clouds by Crystal–Crystal Collision, [https://doi.org/10.1175/1520-0469\(1978\)035<2168:tgosip>2.0.co;2](https://doi.org/10.1175/1520-0469(1978)035<2168:tgosip>2.0.co;2), 1978.
- 10 Wernli, H. and Davies, H. C.: A Lagrangian-based analysis of extratropical cyclones. I: The method and some applications, *Quarterly Journal of the Royal Meteorological Society*, 123, 467–489, <https://doi.org/10.1256/smsqj.53810>, 1997.
- Wernli, H. and P., K.: WCBs and TMEs and Their Relationship to ARs, in: *Atmospheric Rivers*, edited by Ralph, F., Dettinger, M., Rutz, J., and Waliser, D., chap. 3.2, pp. XX, 366, Springer International Publishing, <https://doi.org/10.1007/978-3-030-28906-5>, 2020.
- 15 Wernli, H. and Schwierz, C.: Surface Cyclones in the ERA-40 Dataset (1958–2001). Part I: Novel Identification Method and Global Climatology, *Journal of the Atmospheric Sciences*, 63, 2486–2507, <https://doi.org/10.1175/JAS3766.1>, <http://journals.ametsoc.org/doi/abs/10.1175/JAS3766.1>, 2006.
- Wernli, H., Boettcher, M., Joos, H., Miltenberger, A. K., and Spichtinger, P.: A trajectory-based classification of ERA-Interim ice clouds in the region of the North Atlantic storm track, *Geophysical Research Letters*, 43, 6657–6664, <https://doi.org/10.1002/2016GL068922>, 2016.
- 20 Yano, J.-I. and Phillips, V. T. J.: Ice–Ice Collisions: An Ice Multiplication Process in Atmospheric Clouds, *Journal of the Atmospheric Sciences*, 68, 322–333, <https://doi.org/10.1175/2010JAS3607.1>, <http://journals.ametsoc.org/doi/abs/10.1175/2010JAS3607.1>, 2011.

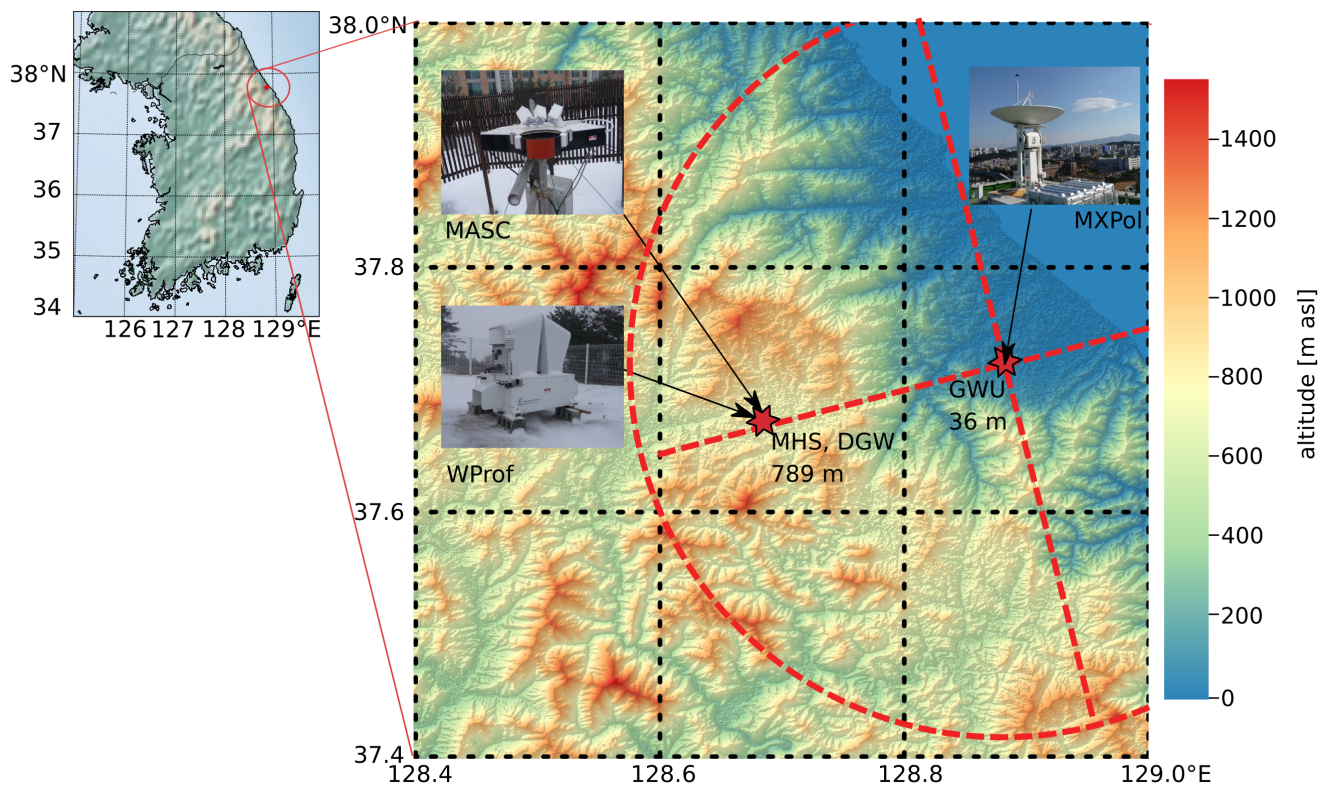


**Figure 1.** Location of the main measurements sites of ICE-POP 2018 used in this study. A digital elevation model shows the topography of the region and its location within South Korea. The red dotted lines and circle show the extent of the main RHIs (27.2 km and PPI (28.4 km radius) respectively.

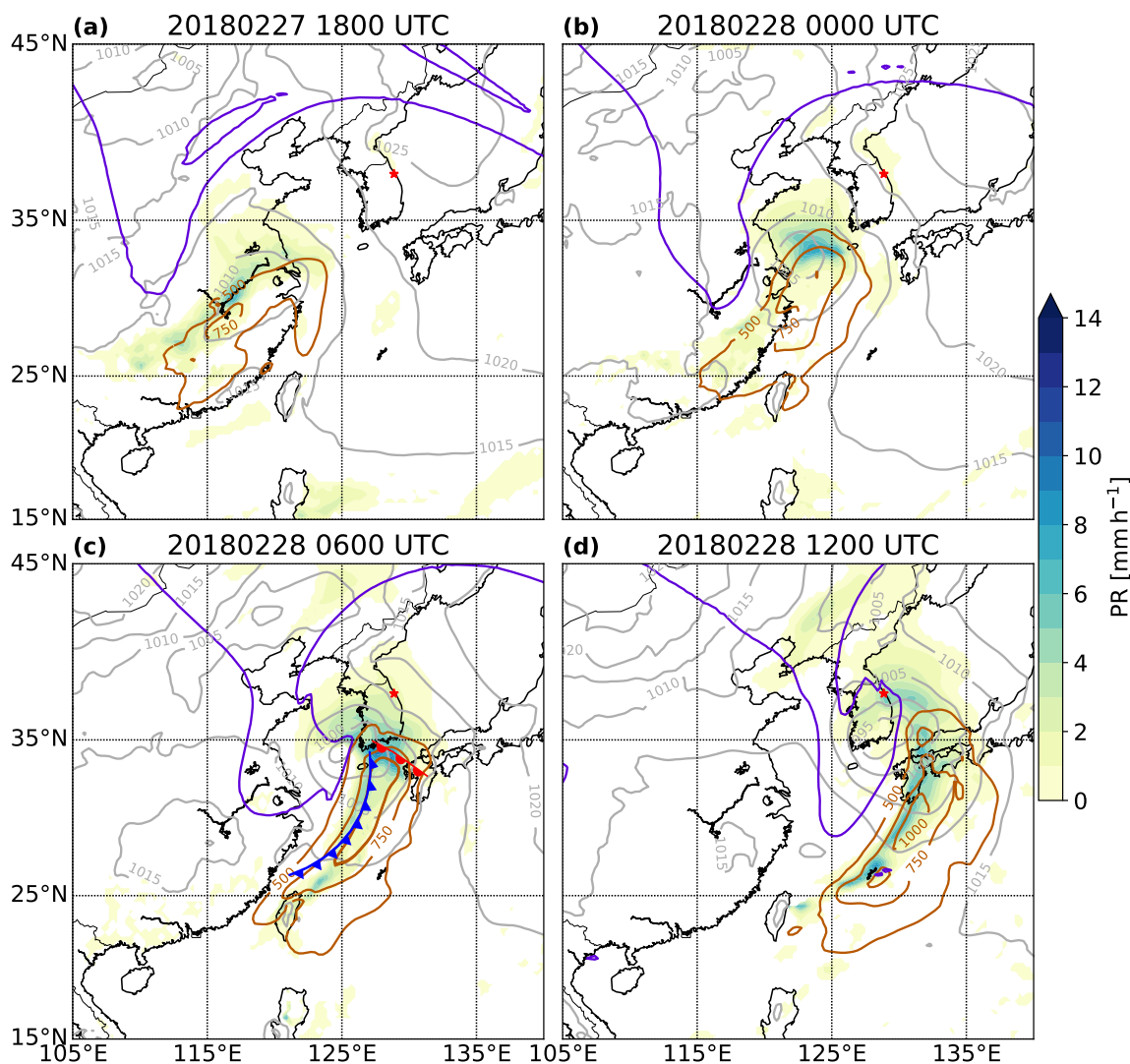


**Figure 2.** Sea level pressure (grey contours, labels in hPa), dynamical tropopause on the 315 K isentropic (purple line), IVT (brown contours, labels in  $\text{kg m}^{-1} \text{s}^{-1}$ , only values greater than  $500 \text{ kg m}^{-1} \text{s}^{-1}$  are shown), precipitation rate (PR) in  $\text{mm h}^{-1}$  (colour filled) at (a) 18:00 UTC 27 February 2018 (b) 00:00 UTC, (c) 06:00 UTC, (d) 12:00 UTC 28 February 2018 from ERA5 data. The warm and cold fronts at 06:00 UTC were manually drawn based on an analysis of equivalent potential temperature on 850 hPa. The red star shows the location of GWU.

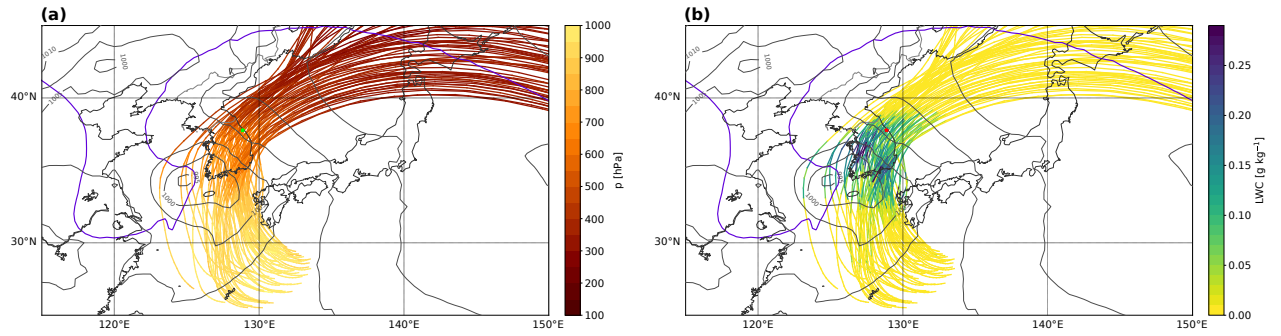


**Figure 3.** WCB trajectories with an ascent rate of at least 600 hPa in 48 h that are located near the measurement site at 06:00 UTC 28 February 2018. Colours indicate (a) the pressure level and (b) the LWC along the WCB air parcels. Also shown is sea level pressure (grey contours, every 5 hPa) and the dynamical tropopause at 315 K (purple). Only the WCB trajectories close to the site (green asterisk on (a) and red on (b)) are shown.

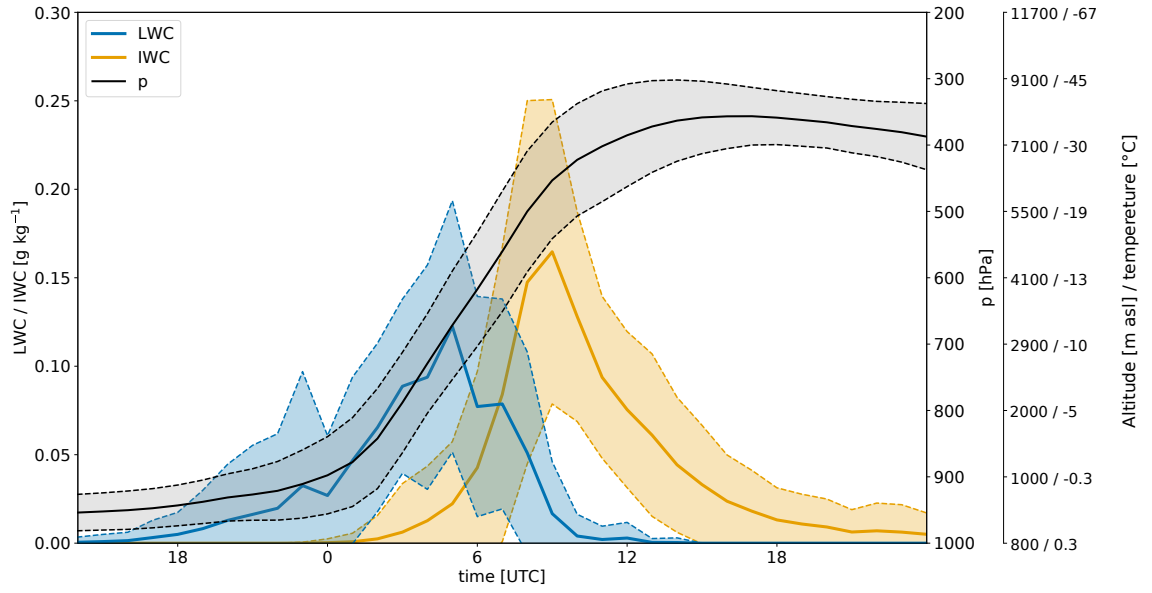


**Figure 4.** Temporal evolution of LWC (blue line, in  $\text{g kg}^{-1}$ ) and ice water contents (IWC, yellow line, in  $\text{g kg}^{-1}$ ) from IFS analyses along the WCB trajectories (black line and grey shading represent the pressure level of the selected trajectories, in hPa) shown in Fig. 3. Shown are the mean (solid lines) and the standard deviation (dashed lines and shading). The altitudes and temperatures of the pressure levels (second right y-axis) are taken from the radiosounding at 06:00 UTC.

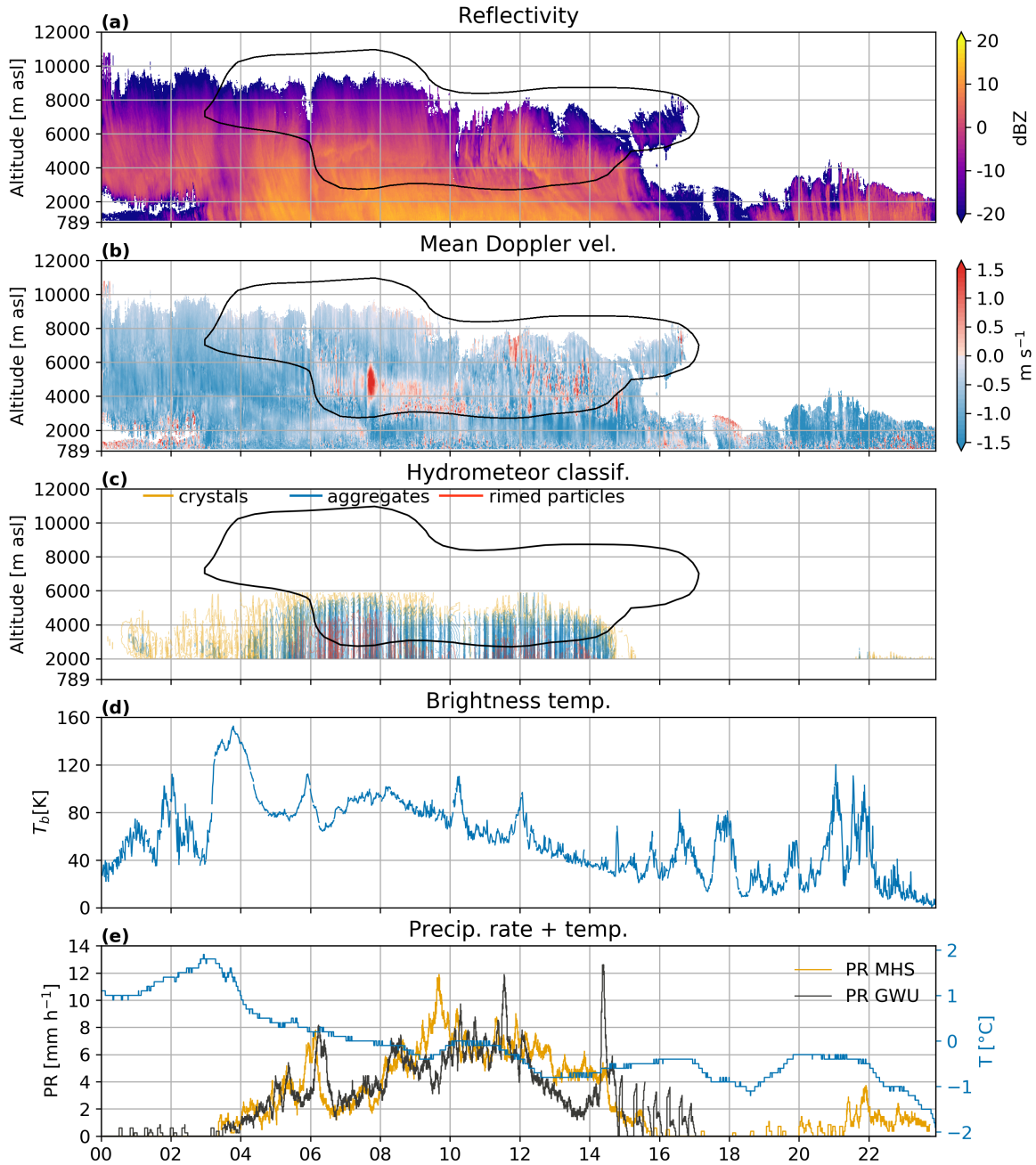


**Figure 5.** Time series on 28 February 2018 of (a) reflectivity and (b) mean Doppler velocity from WProf (defined positive upwards), (c) hydrometeor classification (Besic et al., 2018) based on MXPOL RHs towards MHS. Only data with an elevation angle between  $5^\circ$  and  $45^\circ$  are considered. The isolines represent the proportion of each hydrometeor class normalised by the average number of pixels per time step. The contour interval is 2 %. The yellow contours represent crystals, the blue ones aggregates and the red ones rimed particles. The results are shown only above 2000 m since the lower altitudes are contaminated by ground echoes. The black contour on panels (a), (b) and (c) shows the boundary of the WCB based on the projection of the trajectories in an Eulerian reference frame (see Sect. 2.4). (d) Brightness temperature ( $T_b$ ) from the radiometer, (e) precipitation rate (PR,  $25^{\circ}$  weighing rain gauge) in MHS (yellow) and GWU (black) and temperature in MHS (blue).

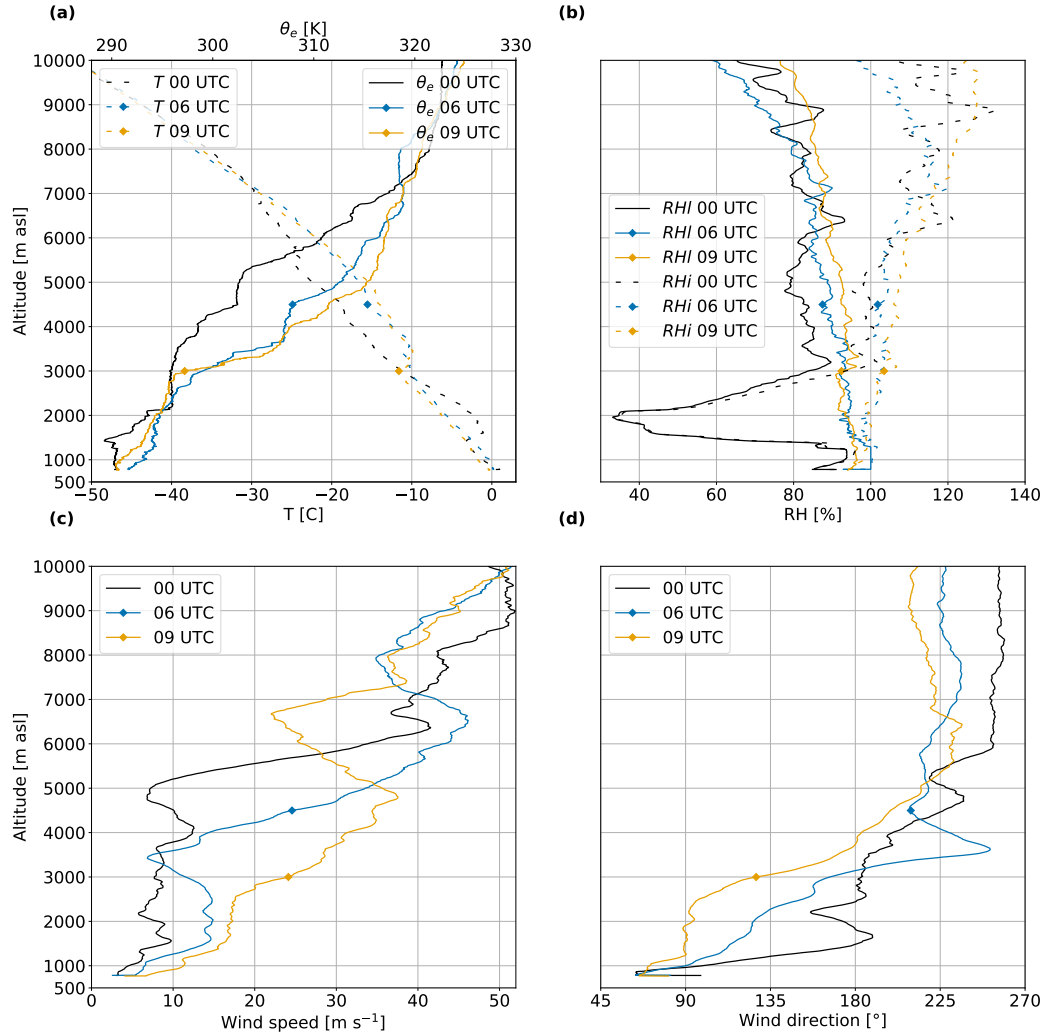


**Figure 6.** Radiosoundings at DGW station showing (a) temperature (dashed lines) and equivalent potential temperature (solid lines), (b) relative humidity with respect to liquid (RHL, solid lines) and ice (RHi, dashed lines), (c) wind speed and (d) wind direction at 00:00 UTC (black), 06:00 UTC (cerise) and 09:00 UTC (blue) 28 February 2018. The diamonds symbols for the radiosoundings at 06:00 and 09:00 UTC show the altitude of the lower limit of the WCB (black contour in Fig. 5a,b,c).

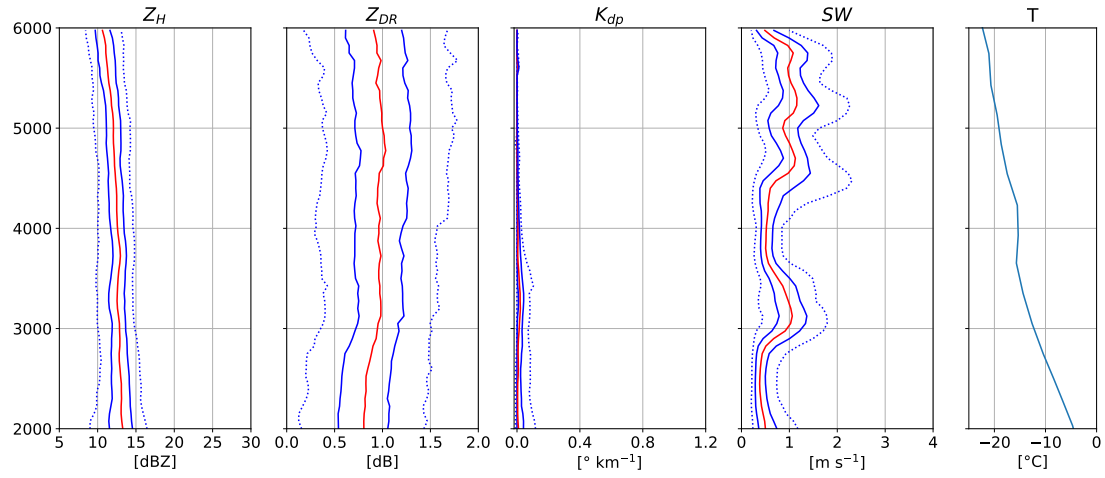


**Figure 7.** Vertical profiles of quantiles of  $Z_H$ ,  $Z_{DR}$ ,  $K_{dp}$  and  $SW$  from MXPOL from 03:00 to 04:00 UTC 28 February 2018. The red line shows the median, while the blue solid lines show the 25th and 75th percentiles and the blue dotted lines the 5th and 95th percentiles. The statistics are based on 11 RHIs towards the MHS site. The data within an horizontal distance of 7 to 20 km from MXPOL is selected. The black dashed line shows the lower limit of the WCB (black contour in Fig. 5a,b,c).

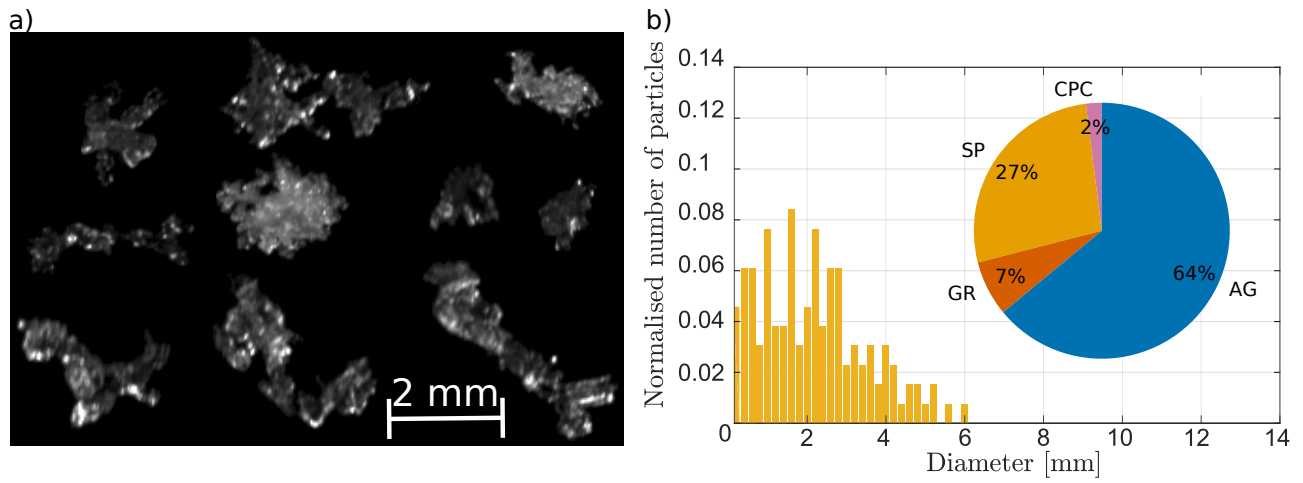


**Figure 8.** (a) Selection of in-focus MASC images. (b) Normalised size distribution and classification of 55 particles observed from 03:00 to 04:00 UTC. SP are small particles, CC columnar crystals, PC planar crystals, AG aggregates, GR graupel and CPC combination of planar and columnar crystals. The size distribution is normalised by the number of particles. The pictures of panel (a) were selected to be representative of the classification. The average temperature was 1.5 °C (Fig. 5e).

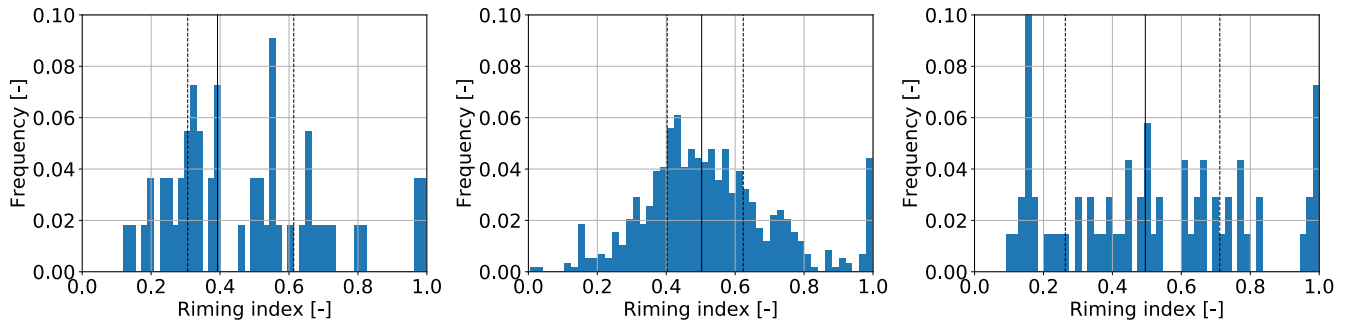


**Figure 9.** Distribution of the riming index for all particles between 03:00–04:00 UTC (a), 06:00–08:00 UTC (b) and 09:00–11:00 UTC (c). The dashed lines show the lower and upper quartiles, the solid line shows the median of the distribution.

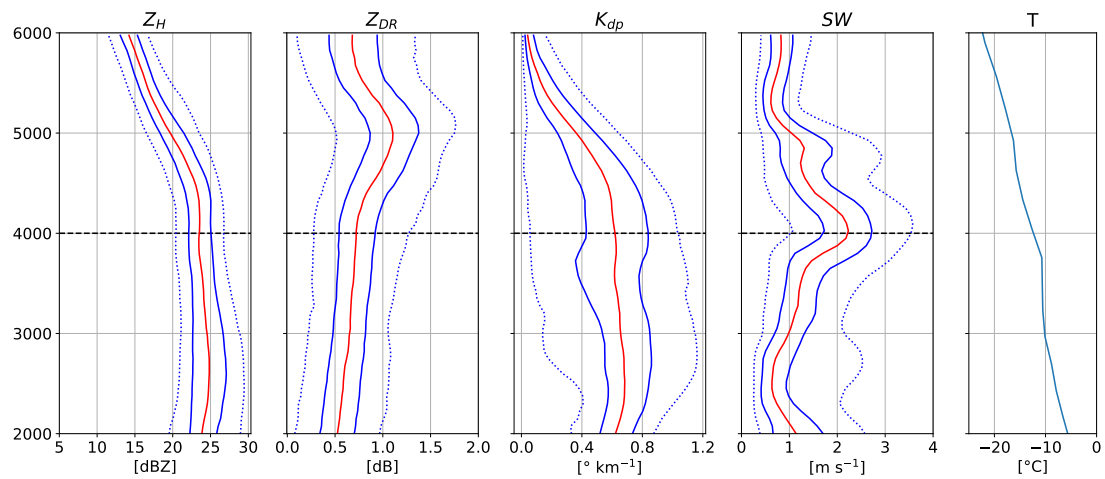


**Figure 10.** Same as Fig. 7 for 06:00 to 08:00 UTC 28 February 2018. The statistics are based on 21 RHIs towards the MHS site. The black dashed line shows the lower limit of the WCB (black contour in Fig. 5a,b,c).

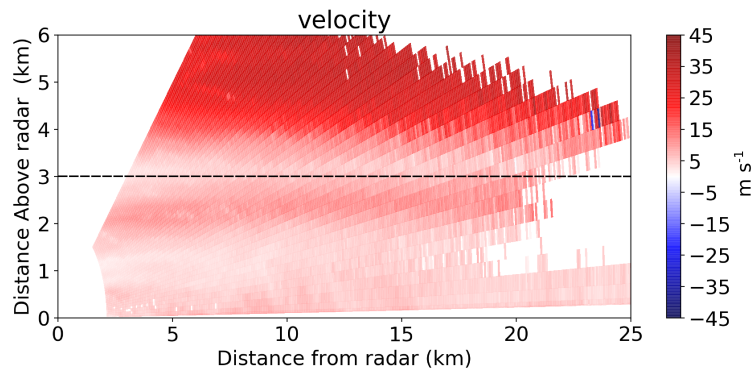


**Figure 11.** RHI of Doppler velocity at 11° azimuth at 06:25 UTC from MXPoI radar. The black dashed line shows the lower limit of the WCB (black contour in Fig. 5a,b,c). The Python ARM Radar Toolkit (Py-ART) Helmus and Collis, 2016 was used to plot the radar data.

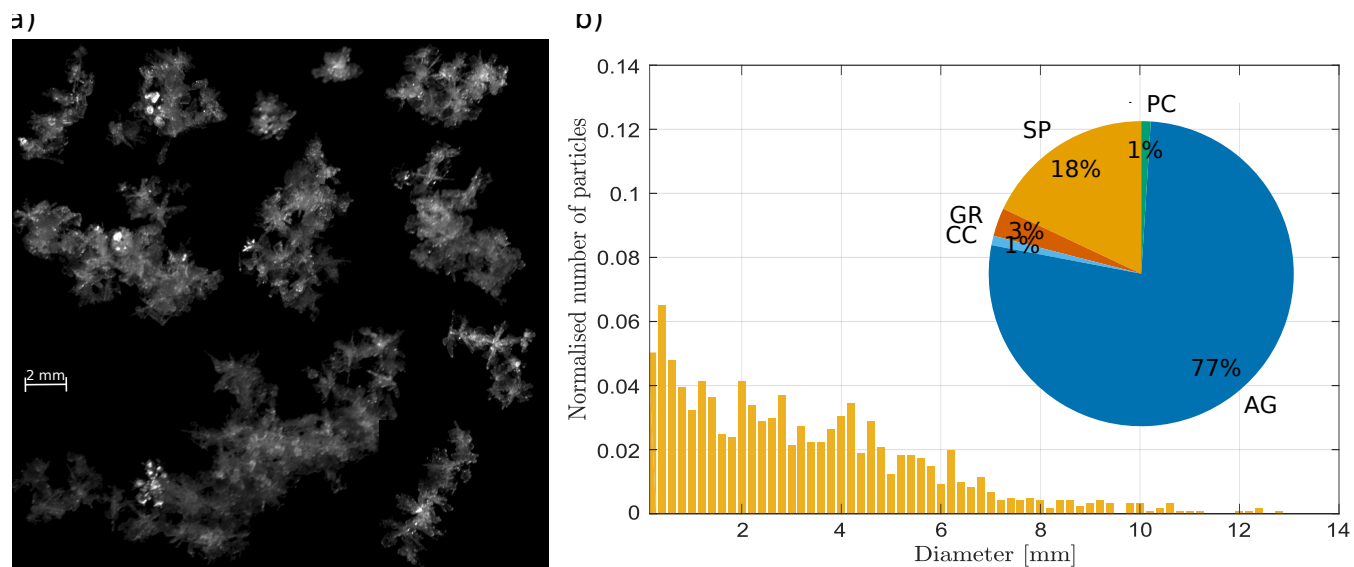


**Figure 12.** Same as Fig. 8 for the period 06:00 to 08:00 UTC. The number of particles is 589. The average temperature was  $0.1^{\circ}\text{C}$  (Fig. 5e).

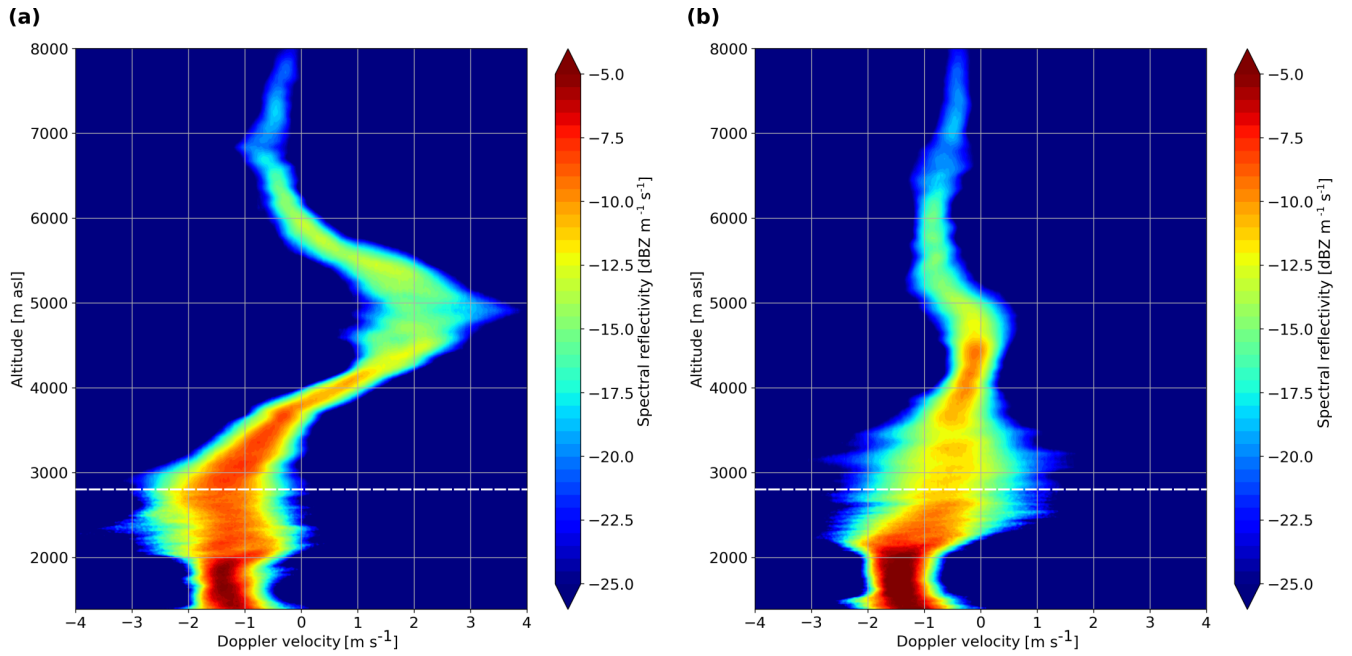


**Figure 13.** Range spectrogram from WProf averaged from 07:42 UTC to 07:47 UTC (a) and from 07:57 UTC to 08:02 UTC (b). Positive velocity values represent upward motions. The white dashed line shows the lower limit of the WCB (black contour in Fig. 5a,b,c).

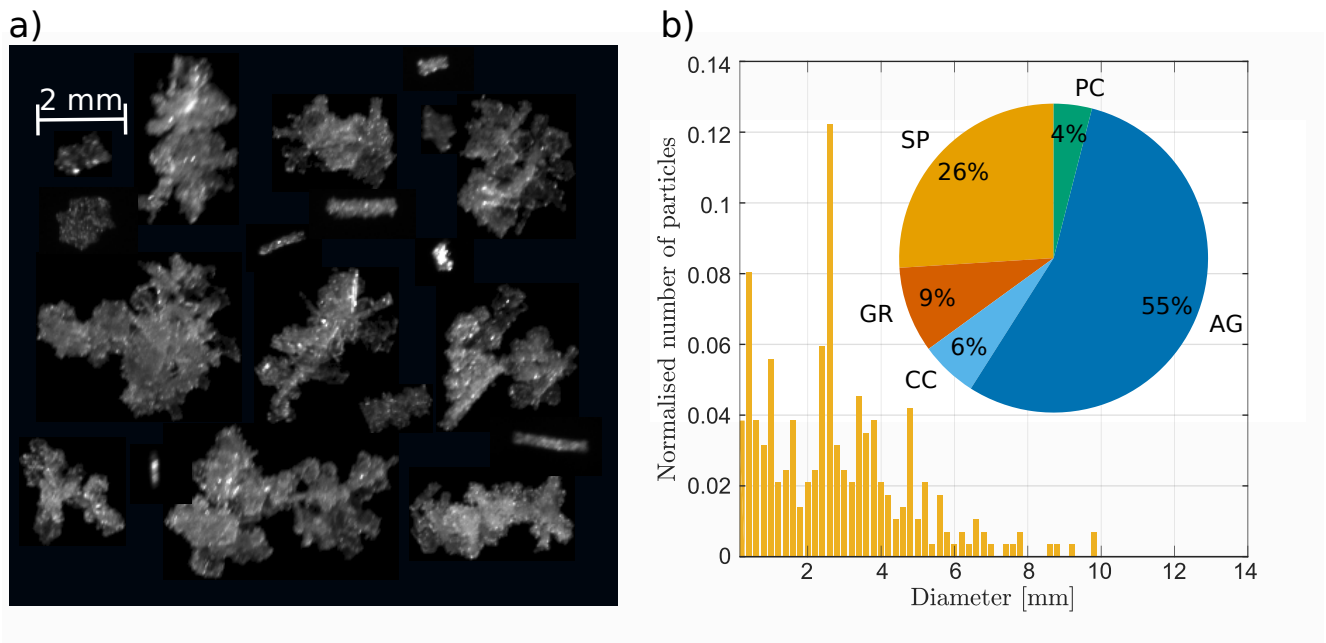


**Figure 14.** Same as Fig. 8 for the period 10:00 to 11:00 UTC. The number of particles is 69. The average temperature was 0.0 °C (Fig. 5e).

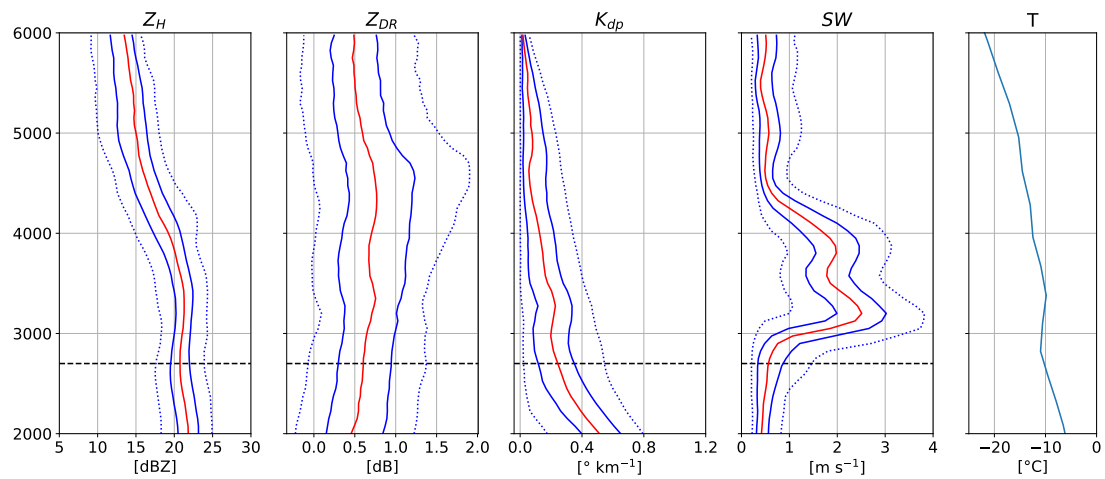


**Figure 15.** Same as Fig. 7 for 09:00 to 11:00 UTC 28 February 2018. The statistics are based on 20 RHIs towards the MHS site. The black dashed line shows the lower limit of the WCB (black contour in Fig. 5a,b,c).

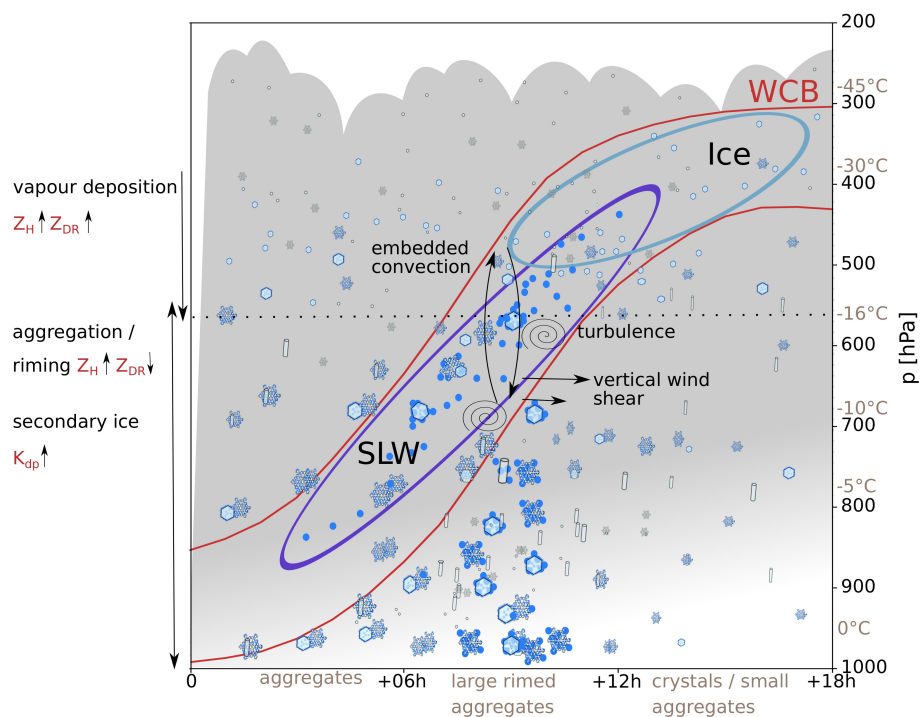


**Figure 16.** Conceptual model in a Lagrangian reference frame (i.e. along the WCB) summarising the key findings. The temperature indications come from the radiosounding at 06:00 UTC (Fig. 6a). The time is indicated as hours from the start of the ascent. The ascent is representative of a strong wintertime WCB.

**Table 1.** Description of WProf chirps

|               | <b>Range</b>   | <b>Range resolution</b> | <b>Doppler interval</b>          | <b>Doppler resolution</b> |
|---------------|----------------|-------------------------|----------------------------------|---------------------------|
| <b>chirp2</b> | [2016, 9984] m | 32.5 m                  | $[-5.1, 5.1] \text{ m s}^{-1}$   | $0.020 \text{ m s}^{-1}$  |
| <b>chirp1</b> | [603, 1990] m  | 11.2 m                  | $[-5.1, 5.1] \text{ m s}^{-1}$   | $0.020 \text{ m s}^{-1}$  |
| <b>chirp0</b> | [100, 598] m   | 5.6 m                   | $[-7.16, 7.13] \text{ m s}^{-1}$ | $0.028 \text{ m s}^{-1}$  |

**Table 2.** Specifications of MXPol and WProf

| Specifications    | MXPol   | WProf                |
|-------------------|---------|----------------------|
| Frequency         | 9.4 GHz | 94 GHz               |
| 3 dB beamwidth    | 1.27°   | 0.53°                |
| Range resolution  | 75 m    | 5.6, 11.2 and 32.5 m |
| transmission type | pulsed  | FMCW                 |

**Table A1.** Values of the different variables used in the computation of  $U_z^*$ . Data from IFS analysis and radiosoundings at 09:00 UTC are used. The pressure  $p$  used is 610 hPa temperature  $T$  is -13 °C

| Variable  | Value                                  | Source   |
|-----------|--|--|
| $q_i$     | $1 \cdot 10^{-4} \text{ kg kg}^{-1}$   | from IFS analysis Fig 4  |
| $q_s$     | $6.5 \cdot 10^{-4} \text{ kg kg}^{-1}$ | from IFS analysis  |
| $\rho_i$  | $920 \text{ kg m}^{-3}$                | density of ice   |
| $\rho$    | $0.82 \text{ kg m}^{-3}$               | At $p = 610 \text{ hPa}$ , $T = -13 \text{ }^\circ\text{C}$ and $RHl = 95\%$ |
| $e_{si}$  | 198 Pa                                 | At $p = 610 \text{ hPa}$ , $T = -13 \text{ }^\circ\text{C}$ and $RHl = 95\%$ |
| $e_{sl}$  | 224 Pa                                 | At $p = 610 \text{ hPa}$ , $T = -13 \text{ }^\circ\text{C}$ and $RHl = 95\%$ |
| $N_i$     | $2895 \text{ m}^{-3}$                  | Eq. A1   |
| $\Lambda$ | 804                                    | Eq. A3   |
| $N_s$     | $2490 \text{ m}^{-3}$                  | Eq. A2   |
| $r_{tot}$ | 309 $\mu\text{m}$                      | Eq. A7   |